applied sciences

MDPI

Article

New Validation Methodology of an Adaptive Wing for UAV S45 for Fuel Reduction and Climate Improvement

Manuel Flores Salinas, Ruxandra Mihaela Botez * and Guy Gauthier

LARCASE Laboratory of Applied Research in Active Control, Avionics and Aeroservoelasticity, École de Technologie Supérieure, Montreal, QC H3C 1K3, Canada
* Correspondence: ruxandra.botez@etsmtl.ca

Abstract: New knowledge in multidisciplinary methodology is presented in this article for the design, aerodynamic optimization, and model validation of an adaptive wing prototype. The optimization framework integrates the design, the finite element analysis, and the model validation. A computational fluid dynamics model of the adaptive wing and the flow in its vicinity was developed and validated with experimental metrics, such as the lift, the drag, and the lift-to-drag ratio. A new genetic algorithm strategy was chosen to find the optimized airfoil shapes for the prototype's upper surface. The reliability of the proposed methodology was investigated through the design, manufacture, and testing of a wing prototype proposed for the UAV S45. The experimental and simulated results have shown a low drag production and a high lift-to-drag ratio of the adaptive wing prototype that will translate into a reduction in fuel consumption and an increase in cruising flight range and therefore into climate improvement.

Keywords: adaptive wing; design; CFD analysis; model validation techniques; wind tunnel test

check for updates

Citation: Salinas, M.F.; Botez, R.M.; Gauthier, G. New Validation Methodology of an Adaptive Wing for UAV S45 for Fuel Reduction and Climate Improvement. *Appl. Sci.* **2023**, *13*, 1799. https://doi.org/10.3390/app13031799

Academic Editor: Wei Huang

Received: 20 November 2022
Revised: 18 January 2023
Accepted: 27 January 2023
Published: 30 January 2023

1. Introduction and Literature Survey

Aerodynamics and structures have motivated aircraft designers to apply new methodologies for reducing fuel consumption and increasing the cruising flight time of unmanned aerial vehicles (UAVs). To improve wing efficiency, researchers have investigated lifting surface optimal configurations by performing aero-structural optimization [1]. The aircraft structure was designed to give optimum cruise performance while withstanding the critical loads corresponding to other flight conditions. These studies in aerodynamic analysis have shown that wing optimization should be considered as early as possible in the UAV design process to optimize the overall performance [2]. It is expected that adaptive wing technologies will become essential in the future of UAV design due to the development of improved aeroelastic concepts in UAV structures and the introduction of new materials with high strength and a high stiffness-to-weight ratio, such as polymer materials [3]. These adaptive wing structures and new materials pose a considerable modelling challenge as they involve highly coupled and nonlinear interactions between the aerodynamic and the structural dynamics [4].

1.1. Wing Design Methodologies

The high level of interaction between the rigid-body dynamics and the structural dynamics poses a significant challenge to a successful actuation of wing system design. Aircraft structures must sustain significant loading variations when flying through turbulence and must suppress catastrophic aeroelastic phenomena such as flutter. One of the earliest works in the field of wing design was performed by Suzuki [5], who minimized wing structural weight by designing the structure and the control system simultaneously. An aeroservoelastic design framework was also presented by Haghighat et al. [6], who considered the interactions between the aircraft structure and the control system. The

structural and the control optimization were performed separately. The same authors also considered maneuver load inaccuracies and their effects on optimum design.

In a traditional design process, the aircraft configuration is first designed, followed by the control system design; this prevents the flight control system from affecting the aircraft configuration [7]. It has been shown that by designing the aircraft configuration and the actuation control system (for the adaptive wing) concurrently these two design optimizations can improve aircraft performance [8].

A variety of modeling and simulation methods to implement and solve the wing optimization problems are available in the literature. These methods can be classified according to their level of fidelity or the degree to which a model or a simulation reproduces the state and behavior of a real-world object [9]. For aerodynamic analysis, the fidelity levels result from different simplification degrees applied to the Navier–Stokes (NS) equations, from the Reynolds-averaged Navier–Stokes (RANS) down to the potential flow theory methods, such as the vortex lattice method (VLM) and the lifting line theory (LLT) [10].

1.2. Adaptive Wing

The ability of a wing to change its shape during flight has been a significant area of interest over the years for both researchers and aircraft designers. Moreover, the adaptive wing can be used to further optimize an aircraft's flight throughout all phases of its typical flight mission by providing significant drag reduction during the climb, descent, and cruise regimes. Flight tests have demonstrated that a 20% reduction in the overall drag of an aircraft leads to an 18% reduction in fuel consumption [11]. The design of the active aeroelastic wing was based on modifying the wing of an existing aircraft in order to make it lighter and more flexible, thereby increasing the aircraft's dynamic performance.

In 1980, with developments in morphing aircraft already a goal for both academia and major aeronautics companies, Boeing modified an existing military aircraft with an adaptive wing structure able to alter its curvature during flight, thereby optimizing its aerodynamic performance for various flight conditions [12]. The Adaptive Wing project, carried out by EADS (European Aeronautic Defense and Space Company), Airbus, Daimler, and DLR (German Aerospace Center) [13], developed a compliant wing structure that could redistribute external aerodynamic forces so that it could be morphed in predetermined areas while remaining rigid to deformation in other areas. In 2001, researchers from NASA Dryden Flight Research Center conducted several flight tests on a UAV equipped with inflatable wings, whose curvature could be modified by adjusting the pressure input.

Other efforts in adaptive wing design have resulted in a variety of morphing concepts, as reviewed by Sofla et al. [14], who combined conventional flap devices with morphing technologies and presented promising aerodynamic gains. Since the early 2000s, adaptive wings have been studied at our Laboratory of Applied Research in Active Controls, Avionics and AeroServoElasticity (LARCASE) at the École de technologie supérieure (ÉTS). The team has studied adaptive wing technologies in two large-scale projects of the Consortium of Research and Innovation in Aerospace in Quebec (CRIAQ). Each of these projects has led to the design and manufacturing of prototypes and their experimental wind tunnel tests. Both projects, called CRIAQ 7.1 and CRIAQ MDO 505, were led at ETS in collaboration with Bombardier, Thales, NRC-IAR, and École Polytechnique in Canada. In the CRIAQ 7.1 project [15–17], the deformation of the upper surface of a morphing wing was conducted using "Smart Material Actuators" (SMA) to improve and control the laminarity of the flow past a morphing wing in order to obtain drag reductions of up to 40%. The resulting deformation made it possible to delay the flow transition on the wing. The CRIAQ MDO 505 project [18–20] was to design and validate a morphing wing with a morphing aileron capable of delaying the flow transition at the upper surface of the wing. The prototype was equipped with four electrical actuators to change its upper surface shape. This concept was experimentally validated in the NRC-IAR wind tunnel.

In this article, we developed a multidisciplinary methodology that can consider the interactions between structures, actuators, and aerodynamics. This methodology is capable

of finding the geometry of an airfoil and its internal structure, which allows its shape to be changed for aerodynamic performance maximization. This research covers the study of a new adaptive wing prototype for the UAV S45 Balaam. The main objective of this adaptive wing is to promote large laminar regions on its surface, thereby reducing drag over the cruising flight phase.

A prototype wing with an adaptive leading edge and upper surface was developed for this study. The flow response at the surface of the prototype wing was measured with an aerodynamic scale. The adaptive wing prototype was manufactured in-house using polymer, wood, and aluminum structures and rapid manufacturing techniques. The position of the leading edge and the upper wing surface were simulated in order to generate airfoils. An optimizer (a genetic algorithm) coupled with an airfoil analysis solver (XFoil) was used to determine the aerodynamic coefficients (C_L, C_D) and then to evaluate the fitness function 'lift to drag ratio' of the generated airfoils. The validation data for the CFD model were obtained during wind tunnel tests performed at the Research Laboratory in Active Controls, Avionics and Aeroservoelasticity (LARCASE) at ETS University.

2. Research Objectives

The objectives for this methodology are:

(i) The design and fabrication of an adaptive wing prototype for the S45. The wing prototype shape was optimized while acting on its controlled surfaces.
(ii) The generation and evaluation of the optimized airfoil shapes of the wing's upper surface in terms of the aerodynamic coefficients (C_L, C_D) and fitness function 'lift to drag ratio'.
(iii) The validation of the adaptive wing with the area metric and adjusted R^2 methods.

3. Wind Tunnel Instrumentation and UAV S45

The Open Return Subsonic Wind Tunnel, the unmanned aerial vehicle, and the aerodynamic balance, as well as the instruments used during wind tunnel tests, are described in this section. The LARCASE laboratory at ETS owns the Price–Païdoussis Twelve-Meter Open Return Subsonic Wind Tunnel, shown in Figure 1. This research apparatus, which is used to test wings and diverse types of prototypes, makes it possible to safely perform studies at various flow conditions.

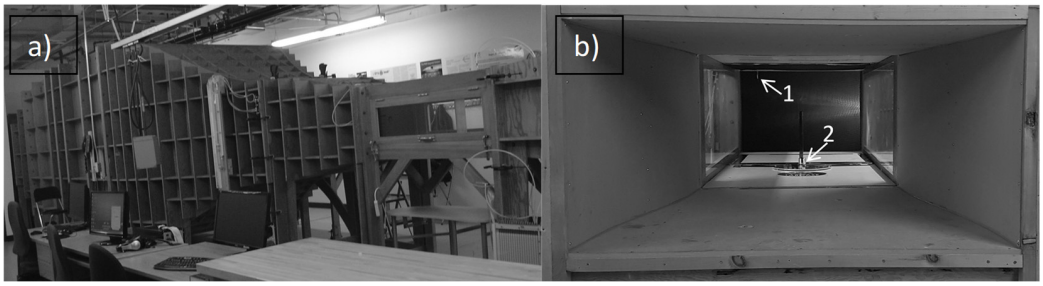

Figure 1. (**a**) The Price–Païdoussis Open Return Subsonic Wind Tunnel. (**b**) Pitot tube location (1) and aerodynamic scale location (2).

The LARCASE wind tunnel consists of a centrifugal fan, a diffusing section, a settling chamber, a contraction section, and a working section. The airflow can develop a maximum speed of 0.18 Mach thanks to the engine and the double impeller centrifugal fan. The two inlets at the opposite side of the rotor allow the air supply to increase the pressure flow, and the 24 small propellers inside each inlet allow the fan to turn at a much higher speed than fans with large blades. The engine and the centrifugal fan are located inside the soundproof mechanical room that protects the wind tunnel from dust particles. The working section is the most critical part of a wind tunnel as that is where the effects of the flow of the wing prototypes are measured. An important step before testing is the calibration of the test chamber that contains the studied model so that the flow conditions inside it can be

monitored [21]. The main parameters to describe the flow in a wind tunnel are the total pressure, the static pressure, the dynamic pressure, the temperature, the flow speeds, and the Reynolds number [22]. These flow conditions can be monitored from the instruments inside the test section. The diffusing section consists of a wide angle diffuser, a large settling chamber, a contraction section, and a test section. The flow goes through a series of five filters; the first is a honeycomb-shaped filter, and the other four are nylon square-shaped filters positioned 0.5 m from each other, as shown in Figure 2. The settling section makes it possible to straighten and to reduce the turbulence in the flow to a turbulence intensity value of 1%.

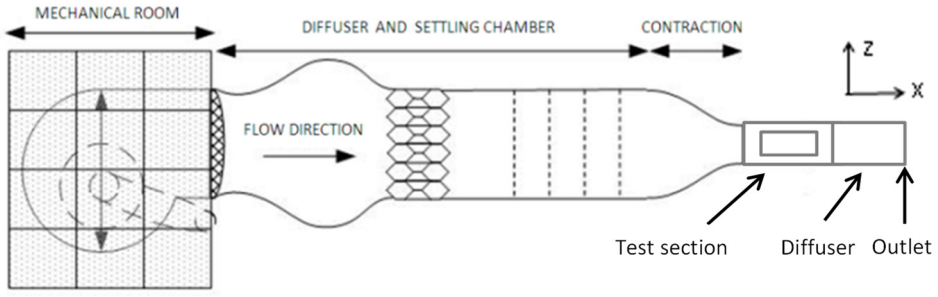

Figure 2. The wind tunnel sections with coordinates.

Figure 3 shows the different dimensions of the wind tunnel sections. Figure 4 shows the design of the wind tunnel sections with the ANSYS ICEM CFD software. Figure 4 shows (a) the settling chamber section, (b) the inlet location, (c) the inner fluid where the wind model is located, (d) the test section and diffuser, and (e) the outlet section.

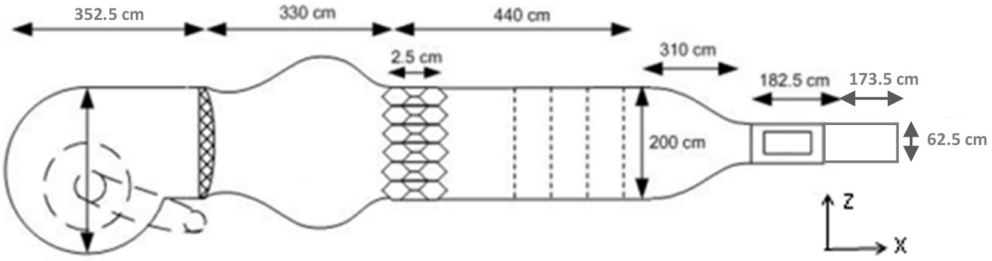

Figure 3. The wind tunnel dimensions in cm.

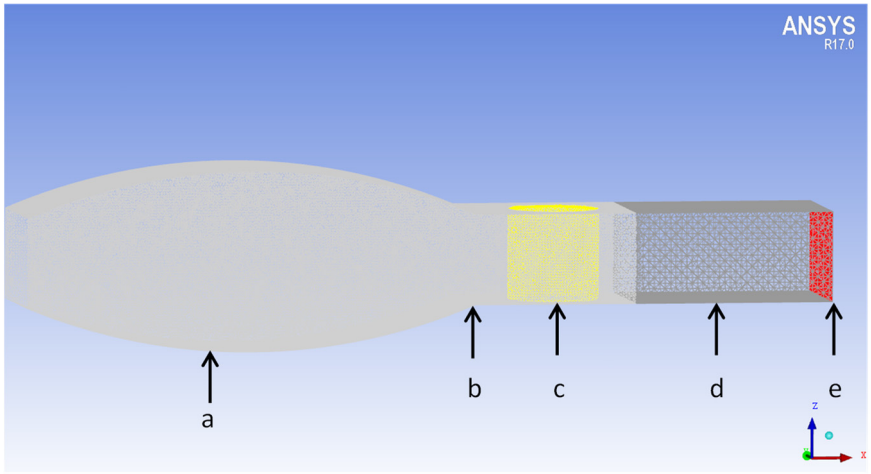

Figure 4. Geometries of the wind tunnel sections in 3D with coordinates: (**a**) the settling chamber section, (**b**) the inlet location, (**c**) the inner fluid where the wind model is located, (**d**) the test section and diffuser, and (**e**) the outlet section.

The S45 is an unmanned aerial vehicle (UAV) manufactured by Hydra Technologies, a company based in Mexico. It serves in Mexico as a surveillance platform for the military, law enforcement, and police agencies. The UAV S45 incorporates a monoplane design with twin tail booms. The airframe is made of lightweight materials, such as carbon fiber, S-glass, and Kevlar. The UAV S45 has the following dimensions: wingspan: 6.11 m; half wingspan: 2.70 m; length from the frontal rotor to the rear rotor: 1.93 m; and tail span: 1.36 m. Its length from the frontal rotor to the tail is 3.094 m, and its wing surface is 2.72 m^2. The UAV's materials are aluminum, titanium, and a composite material (carbon fiber, S-glass, and Kevlar), and its weights are as follows: the operating empty weight (OEW) is 55 Kg; the maximum takeoff weight (MTOW) is 69.4 Kg; the maximum landing weight is 66.50 Kg; and its maximum payload, which is its carrying capacity, is 3.89 Kg. The engines are twin-cylinder of 80 cc with a fuel capacity of 31 L. The main flight specifications of the UAV S45 are its autonomy of 12 h, its maximal operating altitude of 20 000 ft, its operation range of 120 Km, and its cruising speed of 50 kt (25.72 m/s). The UAV S45's main characteristics are indicated in Figure 5, which has numbers corresponding to the propulsion system (1–4), the two Pitot tubes (12,13), and the 10 control surfaces (5–11,14–16).

Figure 5. The aerodynamic and propulsion components of the UAV S45.

The Pitot tube measures the static pressure and the total pressure of the flow. The fluid speed U can be determined by using the air density ρ and the difference between the total pressure P_t and the static pressure P_s, as defined in detail in Section 5.4.

Temperature and humidity readings are important for calculating the air density and its flow rates during experimental testing. The sensor used for measuring the temperature is a thermocouple type-K wire with an accuracy of ± 1 per degree Celsius. The humidity sensor has an accuracy of $\pm 2\%$ at 25 °C. A multifunction data acquisition system from National Instruments (USB-6210) was used to convert the physical forces into digital values that can be interpreted and thus used by the software. The signal measurements were acquired from the aerodynamic balance in order to obtain the signals (Fx, Fy) for the lift and drag force values, respectively, of the adaptive wing prototype.

The measurements of two accelerometer and four actuators signals were performed by a controller installed inside the wing prototype. A custom interface was created to acquire, visualize, and save the aerodynamic balance and the controller data during the wind tunnel tests. The recorded data were imported into the MATLAB software for analysis during the post-processing phase of the project.

4. Multidisciplinary Design, Analysis, and Optimization of an Adaptive Wing

The aerodynamic characteristics of the under-actuated airfoil (wing without actuators) are determined by evaluating the aerodynamics coefficients C_l, C_d and the lift-to-drag ratio, which are also the same parameters used to measure the performance of the new shapes produced by the actuators inside the wing. The airfoil shape configurations are determined through the activation of the actuators and by considering the effects of the actuators and aerodynamic forces acting on the wing's skin simultaneously. The shape of the initial airfoil is defined through a set of parameters determined in the design and manufacturing phases. The configuration and structural properties of the prototype wing's inner structure and the size of the actuators were used to generate a finite element model; in this way, the upper surface of the FE model fit with the desired initial airfoil shape.

The values characterizing the structural properties are directly modified in the finite element FE model, thus allowing the structural and geometrical parameters to be changed simultaneously.

The ability to improve the wing aerodynamic coefficients with internal actuators, and for that system to withstand the aerodynamic forces, is dependent on the size, weight, location, and properties of the wing structure. Additionally, it is necessary to design an underlying structure with reduced stiffness to achieve the needed deformations. This reduced stiffness, however, increases the probability of a structure being influenced by aero-elastic effects (such as flutter).

These challenges drive the need for a multidisciplinary optimization method designed from the early phases of the project, namely preliminary analysis and concept development. The methodology presented in Figure 6 will be followed in this study.

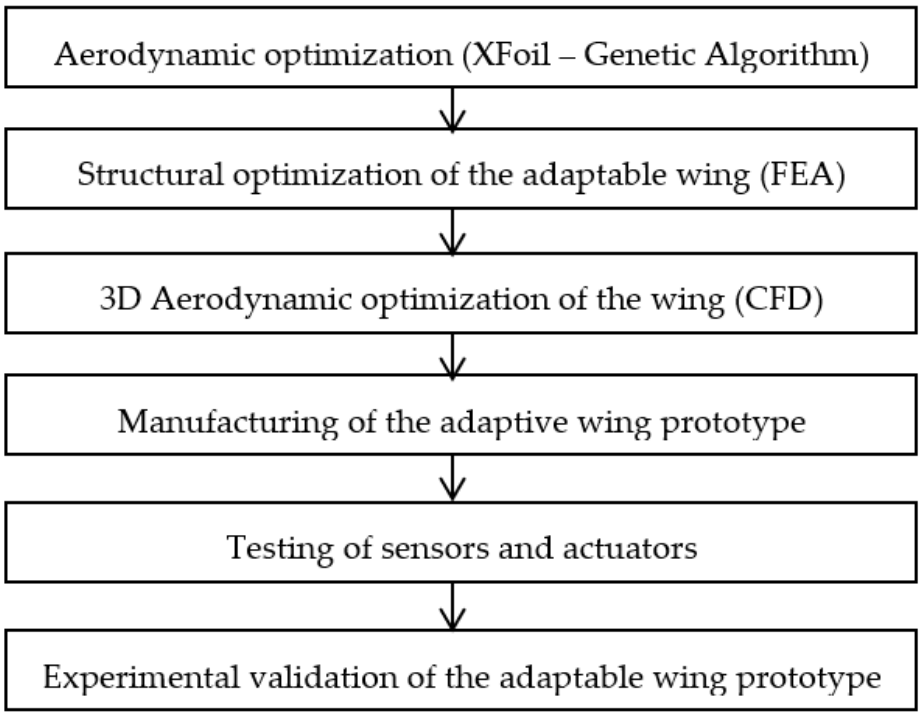

Figure 6. The methodology for the study of an adaptive wing.

The optimization method consists in the coupling of XFoil with the genetic algorithm (GA). The GA routine determines the best spline curve shape passing through the beginning, the middle, and the end of the airfoil geometry. Thus, the coordinates of this spline correspond to the new airfoil shape. These coordinate files (.dat file) are introduced in XFoil to perform the aerodynamic analysis. The optimization method evaluated all of the optimized shapes possible, with a ±5 mm vertical displacement of the actuators. The optimization method can find the optimal shape with the corresponding actuators'

displacements; the optimal shape corresponded to the optimal C_p curve where the transition point was pushed toward the direction of the trailing edge. Delaying or holding back the laminar-to-turbulence flow process has an important impact in drag reduction.

This optimization method allows the real structural deformation shape to be compared with the predicted one given by the GA. When the best shape has been defined, the new airfoil coordinates are tested in XFoil to determine whether the aerodynamic coefficients are better, equal, or worse. The optimization method gives the maximal displacement of the actuators as well as the shape coordinates of the new optimized airfoils.

4.1. Aerodynamic Constraints

The formulation of the aerodynamic constraints for new airfoils is based on the flight conditions. In this paper, only the cruise flight phase of the UAV S45 will be covered. It is assumed that during the cruise flight trajectory the distributions of the lift and drag forces along the wingspan cannot exceed the limitations of the structural loads. The design optimization procedure implicitly defines the following requirements:

(i) The under-actuated airfoil shape will achieve the same lift and drag coefficients as the reference wing requirements;
(ii) The angle of attack will remain constant throughout the cruise flight phase;
(iii) The C_l and C_d improvement (variations) will be achieved through the adaptive system-controlled variation of the airfoil shape;
(iv) Constraints ensure that the airfoil shape remains within the structural and geometrical limitations of the wing prototype. For instance, the wing prototype will have a minimal and maximal allowed vertical displacement (A_{min}, A_{max}) of $\pm$5 mm;
(v) Based on the fitness function definition $f = C_L/C_D$, an airfoil can subsequently be optimized to maximize this objective, and only the best aerodynamically, high-performing new airfoil shapes are experimentally tested in the Price–Païdoussis wind tunnel.

The proposed approach developed at LARCASE to design an adaptive wing considers the interactions between aerodynamics, structures, and control. This multidisciplinary approach is used throughout the design and manufacturing optimization phases of the prototype.

The approach outlined in Figure 7 allows the wing prototype to be designed and optimized with the aerodynamics requirements specific to the S45 cruise flight phase. From these data, the airfoil aerodynamic coefficients are calculated and used as inputs by the subsequent aero-structural optimization to determine the geometrical and structural properties of the airfoil. The key feature of our approach is that the new airfoil shapes are determined by the aero-structural optimization, the structural constraints of the actuators, and the material properties.

4.2. Adaptive Wing Aero-Structural Analysis

A static aero-elastic analysis was performed to obtain the aerodynamic and structural data of the studied model. The structural data include the displacements, stresses, strains, and overall weight. Among the aerodynamic outputs, those of primary interest are the lift and drag coefficients, noted as C_l , C_d, respectively, and the pressure coefficient C_p at the wing upper surface. For the structural solution, the ANSYS software with a nonlinear solver was used.

Design and manufacturing solutions seek to reduce the dynamic aero-elasticity effects. The wing prototype materials are chosen to have high stiffness properties, which is a solution to reduce the occurrence of dynamic instabilities and to delay the occurrence of possible flutter-related phenomena.

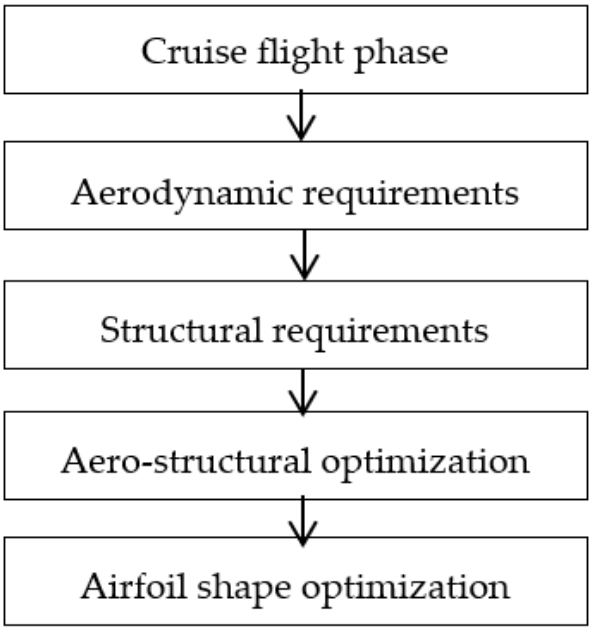

Figure 7. The adaptive wing multidisciplinary optimization methodology.

4.3. Adaptive Wing Actuation Design

The key aspect of the proposed method is that it takes advantage of the interaction between the aerodynamic loads and the structural design of the internal actuators to improve the airfoil's performance. This section describes the wing structure, the actuators, and the finite element modeling.

An adaptive wing was designed to be small and compact so that it could be installed inside the UAV S45 wing; it achieves the required deformations via its distributed hinge-less structure. The compression forces and twisting motions are supported by a redesigned wing box, which allows the decoupling of aerodynamic loads in the spanwise and chordwise directions. This adaptive wing model is designed using a structure composed of segments of different thicknesses connected to its rear spar. When bent under the actuators' force, the space between the plate in the middle and the actuators on the upper surface is filled with polymer foam and honeycomb structures with a high stiffness-to-weight ratio. The compression modulus and dynamic fatigue are properties that assess the foam's ability to support external weight and to retain its reference shape. For instance, when the leading and trailing edge are moving in the downwards direction the bottom half of the material covering the plates will be compressed, while the upper half will be elongated. These two actions lead to an increase in concavity for the inner part and an increase in convexity for the upper part, and thus to an equivalent increase in camber.

Figure 8 shows the FEA of the angular position variation on the leading edge and trailing edge produced by the actuation system. Both the leading and the trailing edge surfaces must be able to move up to 30° in the upward and downward positions.

Figure 9 shows the FEA results measured in terms of stress (in MPa) on the actuation system "arm" and "fixation" at different angular positions of the airfoil leading edge and trailing edge. This evaluation was necessary to validate that the actuation system can displace/move the leading edge and the trailing edge when the airflow is moving at a speed of 30.1 m/s on the prototype surface.

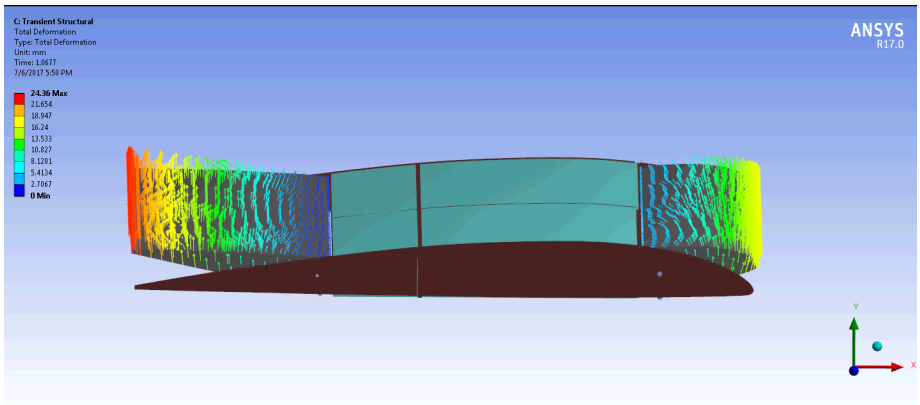

Figure 8. Leading edge and trailing edge angular position variation produced by the actuation system.

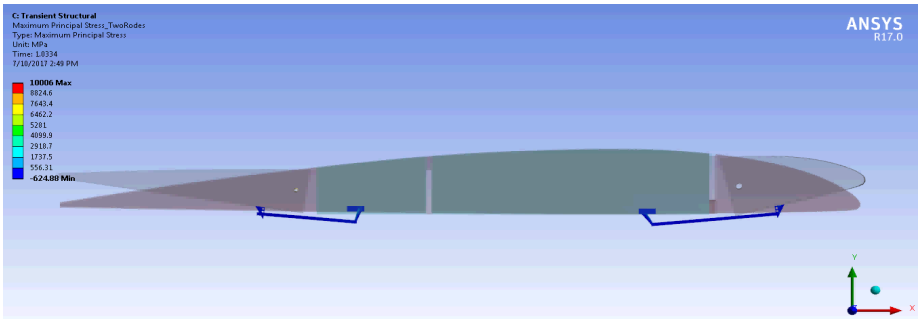

Figure 9. FEA results on the actuation system.

Figure 10 shows the bench test validation of the FEA results for the angular position displacements of the leading edge and trailing edge. This bench test also allowed the validation of the script code written by the main author, and it was used to control the leading edge and trailing edge positions with a feedback signal from the accelerometer inside the wing prototype.

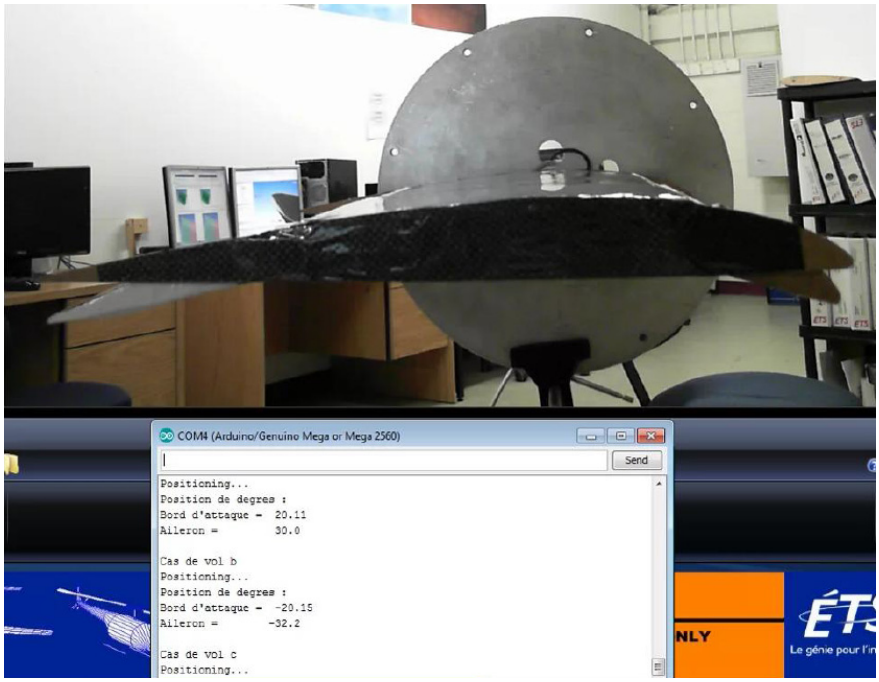

Figure 10. Bench tests of the wing prototype for the FEA results validation.

The UAV wing prototype's actuation is achieved by four servo motor drives that change the wing shape with the structural stresses applied to its polymer skin. The advantages of this skin are the stiffness and the nonlinearity of the material behavior with respect to the stress–strain and to the actuation level-produced force relationships. These actuator motions were modeled in a 3D CAD that considers the results of the structural finite element analyses found with ANSYS FEA software. The following section describes the definition of the goals of the optimizer and the results of the optimization.

4.4. Airfoil Shape Optimization

A genetic algorithm (GA) was used for the generation of new airfoil shapes, starting from their reference shape. This type of algorithm is used in computing to find true or approximate solutions to optimization and search problems and is inspired by the evolutionary principles of biology. The global functioning of genetic algorithms (GA) follows five distinct steps [23]. In the first step, the initial population needs to be created in order to reduce the calculation time. Each individual of this population is a potential solution to the problem. In the second step, the individuals are evaluated in order to create the next generation. The evaluation function is user-defined as the users determine which individuals are selected. In the third step, new individuals are created. Once the best individuals are selected, the new ones are created by "mutation" or "crossover". In the fourth step, the new individuals are added to the population, while the N best individuals of this population are selected. Finally, the fifth step consists of iterating the previous steps until the best solution is found. The evaluation function that defines the evolution of the population is the "fitness function". The GA follows the Darwinian evolution principle via genetic selection and gives valid shapes for almost any combination of parameters characterizing the (i) camber, (ii) location, and (iii) maximum thickness of the airfoils. Certain combinations will be excluded; for instance, high curvature combined with a strong trailing edge deflection can result in undesired airfoil shapes.

The optimization method used on the S45 airfoil is presented in Figure 11. This method is focused on optimizing the upper surface part located between 30% and 67% of the chord. This area was chosen because both the leading edge and the flap zone must not be deformed. A MATLAB script was developed in-house to perform the airfoil optimization by using the class/shape transformation (CST) method to parameterize the airfoil, the ABC algorithm to optimize the shape of the airfoil, and the numerical 2D XFoil solver to run the aerodynamics calculations. Another script was used to run the calculations with the PSO and ABC algorithms and thus to allow the results given by each algorithm to be compared. The optimization method was based on the previous work performed by Koreanschi, Subar, Gabor, et al. [24].

The optimization is applied to the airfoil between 30% and 67% of its chord and is limited to ± 5 mm of displacement in the direction normal to the airfoil.

This study has also been conducted in previous projects at our LARCASE laboratory, where we measured the flow transition point "displacement" in wind tunnel tests with the use of very sensitive pressure sensors (Kulite XCQ_062), which were able to detect the Tollmien–Schlichting frequencies (Project CRIAQ MDO 505).

A new numerical technique was developed at the LARCASE by Popov et al. [15]; it allows the detection of the transition point location using the pressure distribution at the upper surface of the wing (Cp values); the first derivative of the Cp versus the chord variation curve shows the laminar-to-turbulence transition point location using an inflection point in the Cp curve.

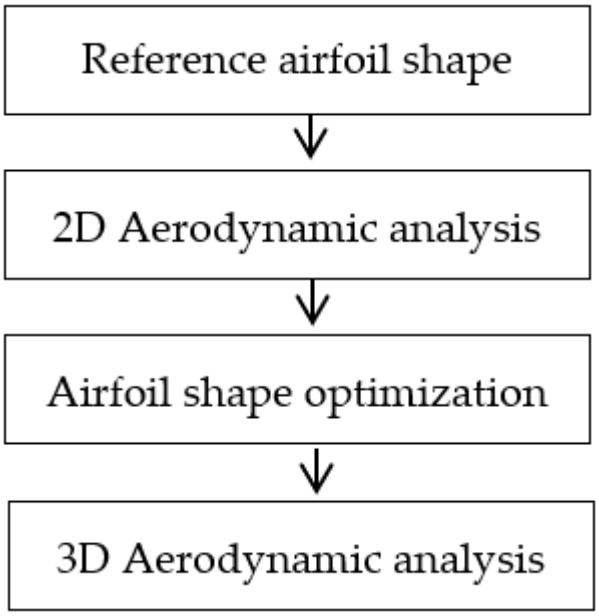

Figure 11. The adaptive airfoil shape optimization methodology.

In our work, the Kulite sensor could not be installed on the wing prototype because it required the drilling of holes on the prototype skin, and the thickness of the skin (of the prototype) was too thin to keep the Kulite sensors "flush mounted", meaning straight and perpendicular to the skin surface.

The Cp variation with the chord was solved with the XFoil software, and the first derivative of the Cp curves was obtained using MATLAB. Figure 12 shows the final particle swarm optimized (PSO) airfoil, which has a transition point delayed to 0.3% of the chord.

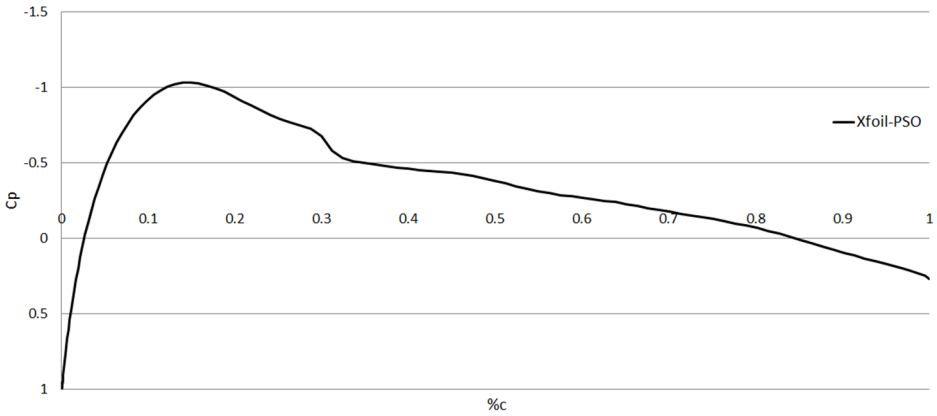

Figure 12. Pressure distribution (Cp) of the optimized airfoil PSO for AOA = 3 for a flow speed of 30.1 m/s.

Figure 13 shows the Cp derivative of a non-optimized (reference) airfoil, with an inflection point located at 0.27% of the chord and the optimized PSO airfoil, with an inflection point delayed to 0.3% of the chord.

The airfoil shape was optimized for angles of attack between 0 and 5 degrees. The parameters used in these algorithms are the size of the colony, the maximum number of iterations, and the number of variables, with the number of iterations fixed at 500.

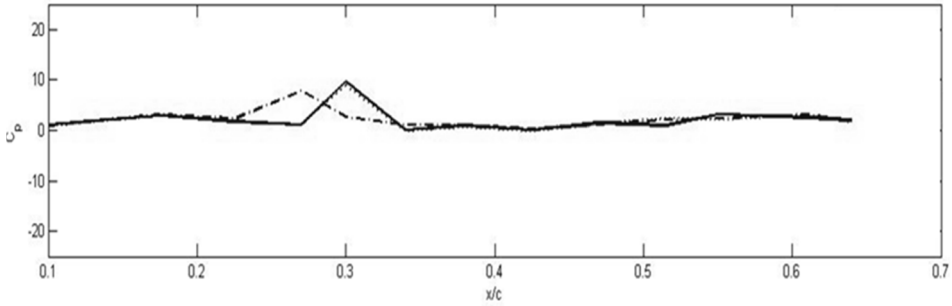

Figure 13. First derivative of the pressure distribution (Cp) of the original (not-optimized) airfoil (short dash line) and the optimized PSO airfoil (solid line).

The aerodynamics conditions are fixed for each airfoil optimization at the cruise altitude of the UAV S45 (2000 ft) and a flight speed of 30.10 m/s. The objective of the optimization is to maximize the fitness function $f = C_L/C_D$, expressed as the lift/drag coefficients ratio, which can be used as an efficiency or a performance factor of the airfoil shapes.

Once the optimization has been performed by each algorithm for each angle of attack between 0 and 5 degrees, it is possible to compare their results. The C_L/C_D are analyzed and compared in Figure 14, where we can observe that the optimized airfoils have improved efficiency for the angle of attack (AOA) between 2° and 4°. The C_L/C_D values for the AoA = 3° were improved by 21% and 26% with the ABC (long dash line) and the PSO (short dash line) algorithms, respectively, when compared to the reference airfoil shape (solid line).

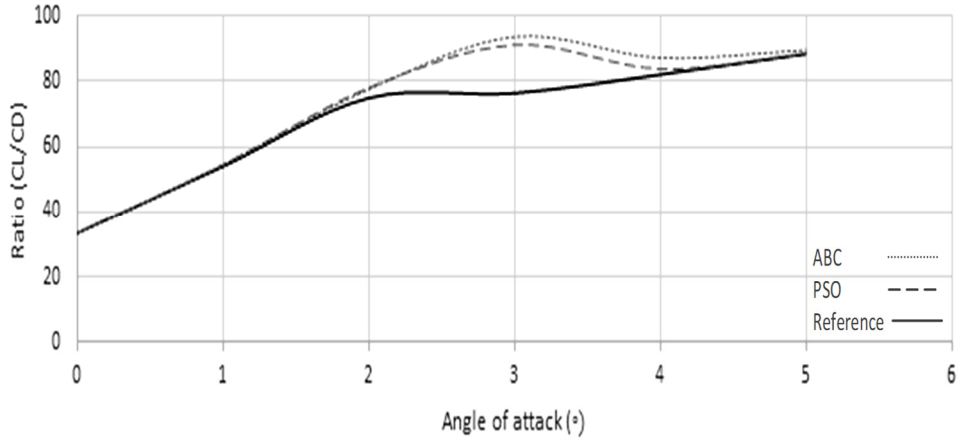

Figure 14. Results of the ABC and PSO optimized airfoils versus original UAV S45 airfoil.

The aerodynamic shape optimization method described in Section 5, coupled with the aero-structural analysis method presented in Section 5.2, together with the airfoil parameterization in Section 5.4, allows for aero-structural optimized airfoil shapes with increased performance.

5. Adaptive Wing Design and Manufacturing

5.1. Adaptive Wing Design

This section describes the design of the adaptive wing on which the surfaces controlled by the actuators are to be installed. The most effective way to alleviate the associated problems with controlled or actuated surfaces is to design the stiffest possible wing box structure, without exceeding the wing weight limitation. The main parameters, such as airfoil section, wing planform area S, wing chord length c, wingspan b, aspect ratio A, and thickness-to-chord ratio t/c, have to be found at the early stages of the aircraft design. For the design of the prototype, the basic wing parameters were defined by the original S45 wing structure, as shown in Figure 15.

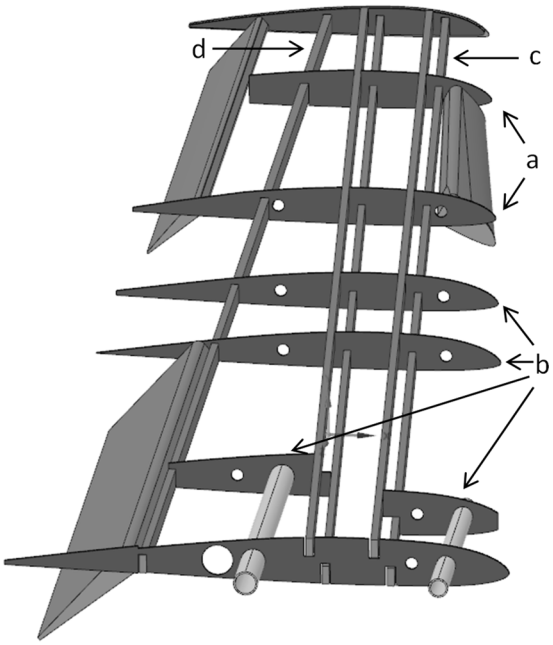

Figure 15. Adaptive wing prototype based on the S45 structure, spanwise view: (**a**) two actuators support ribs, (**b**) three skin support ribs, (**c**) front spar, and (**d**) rear spar.

The wing box design depends on the location and material properties of the spars, ribs, and skin. The prototype wing box should have reinforced spars to support the actuators' push and pull forces. As a single spar cannot sustain the prototype structural stress, another spar was added to the wing box. Wing design approaches indicate that for a two-spar wing, the front spar should be located at between 12 and 17% of the chord if the rear spar is located at between 55 and 60% of the chord [25]. The main reason for these spar locations is to support the pressure distribution and improve the aero-elastic characteristics of the wing prototype.

As described in Section 5, we need to install four actuators to change the airfoil shape. These actuators need support arms to apply their forces to the control surfaces. Therefore, two support ribs for the actuation are needed. In addition, three more ribs are needed to stiffen the front and rear spar relative distortions and to prevent skin buckling, which could lead to an increase in the critical stress threshold of the skin material.

5.2. Adaptive Wing Structural Analysis (FEA)

The structural modeling of the prototype wing is accomplished by using the finite element method (FEM) and ANSYS software. This section describes the selection of the element types, the FEM solid modeling, the part connection, the mesh generation, and the boundary conditions. The most commonly used element type in aerospace is two-dimensional (2D), as the industry is mostly dealing with thin-walled structures. Almost every main structural part can be modeled using this type of element. One-dimensional-type elements on the other hand also have applications for connecting beam-like structures [26,27]. Two-dimensional-type elements are generally chosen for the design of thin-walled structures such as the polymer skin for the wing considered here. The thicknesses of the other parts in the wing box could also be reduced and modeled with 1D-type elements, but for the spars, it was determined that they be modeled using 2D-type elements to obtain more accurate results in the bending responses. The last sets of structural parts are the ribs, which are used to increase the torsional stiffness of the wing structure and to stabilize the skin panels. The resultant stress levels on the ribs, except for the concentrated stresses around the fasteners, are assumed to be very low compared to the stresses on the spars and the skin [28]. Hence, 1D-type elements were assigned to the ribs.

The modeling of the structural parts was conducted by generating surfaces. First, the geometrical model of the composite skin was generated. Second, the surfaces representing the wing box were generated. Third, the ribs were generated in three sections by location. The first section was located at the leading edge section up to the location of the first spar. The second section was located in between the two spars. The last portion starts at the second spar and continues until the trailing edge.

The spar and rib surfaces can be meshed using a meshing technique called 'Iso-Meshing', whereas complex surfaces such as the skin and the wing box can be meshed using the 'Paver Meshing' method [29,30]. The Iso-Meshing method creates elements that have the same angles between edges, but Paver Meshing only keeps the global element edge length defined for the meshing approximately the same, and then, it creates non-symmetrical elements.

There were two sets of connections for the wing. The first one was the connection between the spars and the skin, and the second one was the connection between the ribs and the skin. All the necessary edges for the defined connection sets have been associated with the related surface. The resulting geometry is shown in Figure 16.

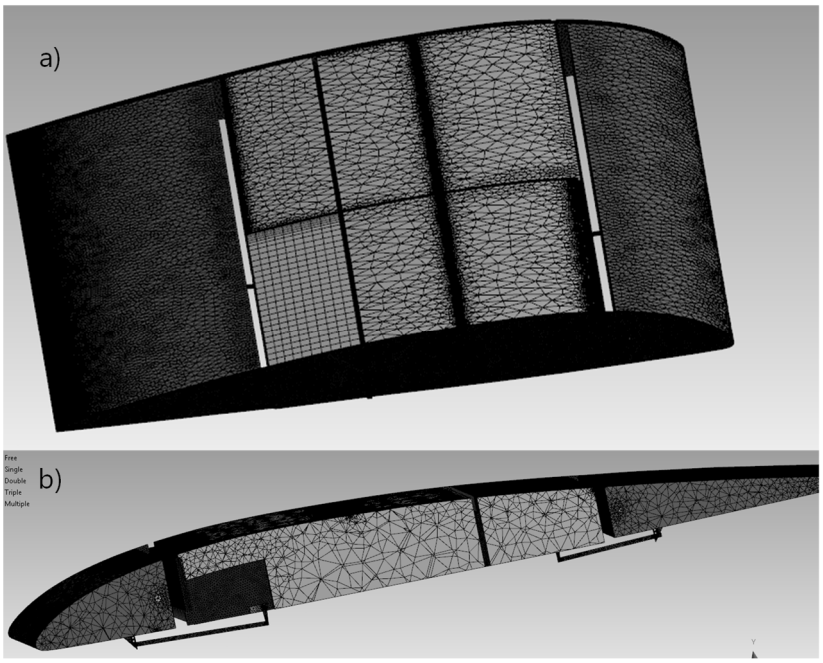

Figure 16. Mesh generation of the adaptive wing: (**a**) top view and (**b**) isometric view.

The purpose of the FE model property updating is to integrate the components of a structure model and their properties. A wing mesh model becomes a structure composed of spars, ribs, and skin, which has specific mechanical properties, material properties, and other information, in addition to the geometrical information. Shape optimization is solved at each iteration. The mesh and the FE model are updated at the same time in the process of the optimization iterations, causing a new round of meshing and physical property loading.

The FE methodology presented in this section allows (i) the generation of the FE model through a CATIA design template. The template interface can achieve rapid model modifications and improvements. (ii) It allows the mesh segmentation of the spars, ribs, and skin, which are divided and meshed separately inside the FE model. (iii) The FE properties and model analysis are loaded on the wing structure after iteration.

The FE model developed in this section was manufactured in-house and is presented in Section 5.3.

5.3. Adaptive Wing In-House Manufacturing

The new wing design must replace the actual rigid wing of the UAV S45; therefore, the new design must have the same span length, a tip chord length of 0.40 m, a base chord length of 0.65 m, and an approximate weight without any instruments of 4.5 kg. The design of the adaptive wing structure has the same internal structure as a rigid wing in the sense that it consists mostly of spar and rib structures. The difference between a rigid wing and an adaptive wing structure is the configuration of the wing box structure to support the actuators.

Rigid wing structures rely on ribs to support the skin and maintain their airfoil shape. In the case of the proposed adaptive wing prototype, the rib structures have to change forms, allowing additional shape variations. These ribs are also intended to support the chordwise bending moments occurring through the pressure differential between the upper and lower surfaces. Furthermore, the ribs provide the sliding mechanism that allows the leading and trailing edge structures to change their shape, as shown in Figure 17. The additional torsional loads are supported by spars located as specified in Section 5.1.

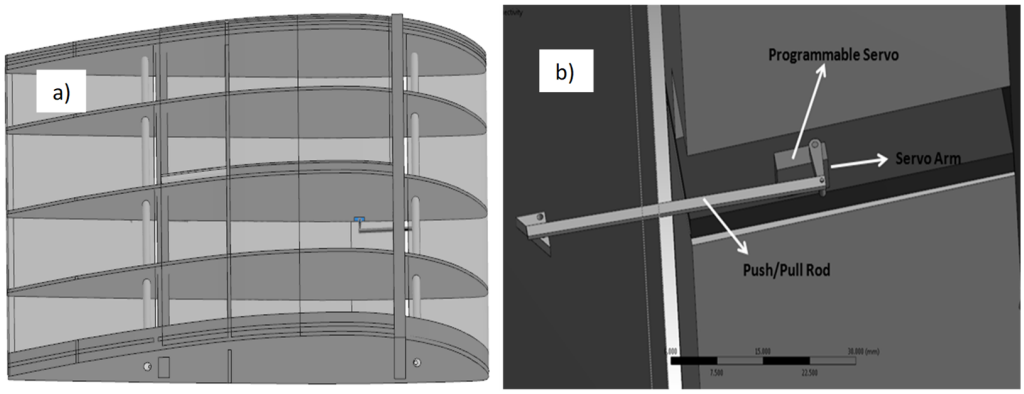

Figure 17. (**a**) Top view of the leading edge adaptive wing prototype; (**b**) actuator design is composed of a servo motor and a push/pull rod.

To manufacture an adaptive wing prototype with improved performances compared to those of the original S45 wing, it is necessary to consider not only the flight phase conditions of the UAV, as presented earlier, but also the additional loads of the actuators. The fabrication of the wing parts requires CAD files and a program supported by Windows operating systems, as well as scripting capabilities. The ANSYS software package allows the CAD design to be exported into files of a format (Step files) that can be used by the FEA and CFD programs. The manufacturing of the adaptive wing was carried out in several stages.

As the scope of this thesis is the design and fabrication of a prototype, further descriptions are given below.

The flexible upper surface or skin used on an adaptive wing prototype must support the surface pressures resulting from the flow over the wing while allowing a controlled wing shape change. Compensation for the additional loads is included in the design of the adaptive wing structure. To obtain the desired optimized shapes, the polymer skin material is incorporated in the design and fabrication of the adaptive wing to allow for a precise and smooth transition during the shape changes. The skin material must have the required structural properties for the flight conditions of the UAV S45 and be able to sustain the original rigidity while allowing a quick transition and a very good recovery force, as the skin must return to its original shape when the adaptive wing system is not functioning. A material with increased modulus and toughness is desired so that the transfer of the surface pressure can proceed with minimal skin deflection. In order for the polymer skin to be stretched to a new configuration, while activated, a specific polymer material with a well-suited modulus value is needed.

Other factors for the selection of the wing skin material are the yield and ultimate strengths, thermal resistance, stiffness, and density. Moreover, the manufacturability, cost, and availability are important factors. Finally, polycarbonate polymer was chosen for the prototype upper surface (skin). The material properties [31] and dimensions are shown in Table 1. The mass ratio is calculated with the equation shown in the last row. A more detailed equation for the mass ratio (μ) is shown here:

$$\mu = \text{Density fluid} \times \text{foil length} / \text{Density foil} \times \text{foil thickness} = 1.225 \times 150\ \text{mm} / 1200 \times 1.02\ \text{mm} = 0.15.$$

Table 1. Polycarbonate polymer properties of the prototype skin.

Skin Properties	
Material	Polycarbonate polymer
Young's Modulus E	2.38 GPa
Poisson ratio v	0.38
Density ρm	1200 kg/m^3
Mass ratio μ	μ = 1.225 × 150/1200 × 1.02 = 0.15

The optimal design of the wing structure involved restrictions for the actuators and a skin support mechanism. These restrictions included the need to house the actuation components within the rib structures to ensure no interference with the skin support structure designed to slide on the rib surface, as shown in Figure 18.

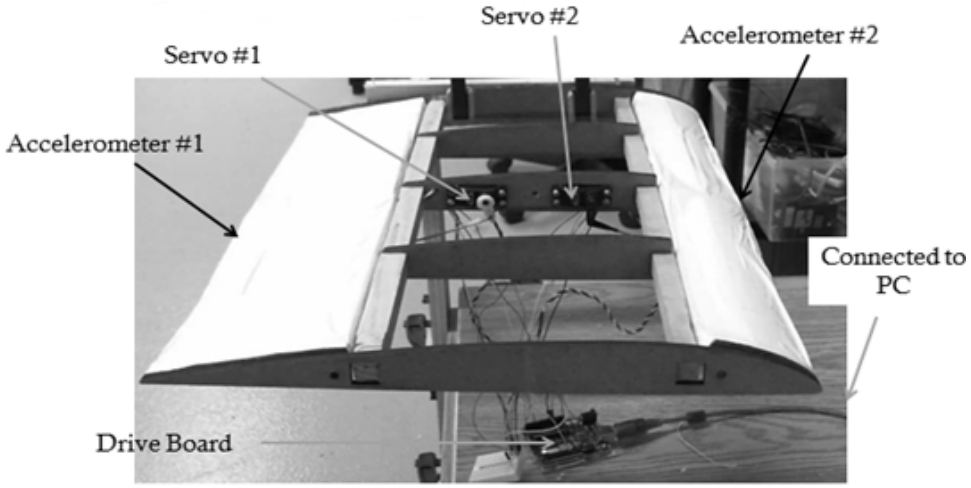

Figure 18. Adaptive wing prototype instrumentation and sensors.

Attaching the skin to the upper wing surface can result in a torsional strength increase for a wing. In the case of this adaptive wing structure, since the skin will change between the rigid and the elastic state, the inner and lower wing structure was sized to compensate for losses in its torsional strength. The manufacturing of the adaptive wing prototype was achieved with a safety factor of 2.0, which is a recommendation by Mehta et al. [22] for wind tunnel testing. The images of the prototype inside the Price–Païdoussis wind tunnel are given in Figure 19.

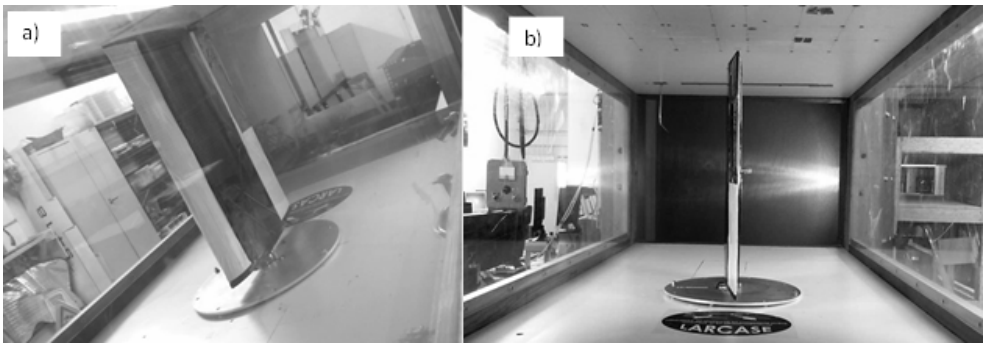

Figure 19. Adaptive wing prototype experimental tests: (**a**) side view and (**b**) back view.

5.4. Dimensional Analysis with Buckingham's Theorem

The "dimensional analysis method" solved with the aid of "Buckingham's theorem" can be a very powerful tool for understanding complex wind tunnel tests [32,33]. Buckingham's theorem is used to analyse the relationships and interactions between the fluid flow and the wing prototype during wind tunnel tests. The physical unit of mass (Kg), the time (s), the length (m), and the temperature (K) are represented by the independent variables M, T, L, and Θ, respectively.

The forces (lift and drag) are determined by the relationships between the 11 input variables, 7 of them defining the fluid, and 4 of them defining the adaptive wing model, as shown in Table 2.

Table 2. Variables for the analysis of the adaptive wing.

	Variables for the Analysis on the Adaptive Wing Prototype	Dimensions
(I)	Input variables representing the fluid in the wind tunnel	
(1)	Density (ρ)	ML^{-3}
(2)	Fluid velocity (U)	LT^{-1}
(3)	Dynamics viscosity of the fluid (μ)	$ML^{-1}\ T^{-1}$
(4)	Temperature of the fluid (t)	Θ
(5)	Static pressure of the fluid (P_s)	$M\ L^{-1}\ T^{-2}$
(6)	Dynamic pressure of the fluid (P_d)	$M\ L^{-1}\ T^{-2}$
(7)	Total pressure of the fluid (P_t)	$M\ L^{-1}\ T^{-2}$
(II)	Input variables representing the adaptive wing prototype	
(1)	Wing chord (c)	L
(2)	Angular displacement of the leading edge (LeadingEdge)	non-dimensional
(3)	Angular displacement of the trailing edge (TrailingEdge)	non-dimensional
(4)	Angle of attack of the wing (AOA)	non-dimensional
(III)	Output variables representing the wind tunnel results	
(1)	Lift force	MLT^{-2}
(2)	Drag force	MLT^{-2}

The Bernoulli Equation (1) allows the expressing of the subsonic fluid velocities (U) with three pressure variables (static, dynamic, and total pressure) and one fluid density (ρ) variable. The three pressure variables can be reduced and their effects expressed by the variable U magnitude.

$$U = \sqrt{\frac{2\left(P_{dym}\right)}{\rho}} \text{ where } P_{dym} = (P_T - P_s) \quad (1)$$

The fluid temperature (T) affects the dynamic viscosity (μ) and the density (ρ) values of the air during wind tunnel tests. The value of the temperature variable (t) is used to define the density and the dynamic viscosity of the air at which the tests will be conducted; therefore, the variable (T) can be reduced in this analysis. The four variables (P_T, P_{dym}, P_s, T) can be excluded from the list of 11 input variables, as their effects are expressed as independent variables (U, ρ). The aerodynamic forces (drag and lift) can be expressed as a function of seven independent input variables, as shown in Equation (2).

$$\text{Force (Lift, Drag)} = f\{\rho\ ,\ U\ ,\ \mu\ ,\ c,\ \text{LeadingEdge},\ \text{TrailingEdge},\ \text{AOA}\} \quad (2)$$

To find the relationships between these seven variables and their effects on the drag and lift forces considered as output (Table 3), we have to use the Buckingham theorem in Equation (2).

Table 3. Variables for the lift and drag analysis.

Variables Specified for the Analysis of the Adaptive Wing Prototype		Dimensions
(I)	Input variables representing the fluid in the wind tunnel	
(1)	Density (ρ)	ML^{-3}
(2)	Fluid velocity (U)	LT^{-1}
(3)	Dynamics viscosity of the fluid (μ)	$ML^{-1}\ T^{-1}$
(4)	Wing chord (c)	L
(5)	Angular displacement of the leading edge (LeadingEdge)	non-dimensional
(6)	Angular displacement of the trailing edge (TrailingEdge)	non-dimensional
(7)	Angle Of Attack of the wing (AOA)	non-dimensional
(II)	Output variables representing the wind tunnel results	
(1)	Lift force	MLT^{-2}
(2)	Drag force	MLT^{-2}

We can observe in Table 3 that all seven input variables and the two output variables can be defined by these three M, L, T physical dimensions. The theorem makes it possible to find the number of π terms (symbolized by the Greek letter π_1 , π_2 , etc.) needed to define the relationships between the input and output variables, which in this case are the drag and lift forces. The first step of the theorem is to remove the number of dimensional parameters from the input and output variables. The non-dimensional input or output variables are excluded in the analysis. For the lift force analysis, there are only four input variables and one output variable. The removal of the physical dimensions from the variables gives a minimum of two π terms for the lift force, as shown in Equation (3):

$$4 \text{ input variables} + 1 \text{ output variable} - 3 \text{ physical dimensions} = 2\ \pi \text{ terms} \quad (3)$$

Next, we separate the dimensional independent input variables and the input variables containing all three physical dimensions (M,L,T), as shown in Table 4.

Table 4. Independent, dependent, and output variables of lift.

Independent Variable Dimensions		Dependent Variable Dimensions and Output Variable of Lift	
Density (ρ)	ML^{-3}	Dynamics viscosity (μ)	$ML^{-1}\ T^{-1}$
Fluid velocity (U)	LT^{-1}	Lift force (F)	MLT^{-2}
Wing chord (c)	L		

The independent variables of the physical dimensions are matched to reduce the lift force (F) physical dimensions; therefore, the first term found is shown in Table 5.

Table 5. Dimensional analysis first term found.

Reduction with the variable: ρ	$\frac{(F)}{(\rho)} = \frac{MLT^{-2}}{ML^{-3}} = \frac{LT^{-2}}{L^{-3}}$
Reduction with the variable: U^2	$\frac{(F)}{(\rho)(U^2)} = \frac{LT^{-2}}{T^{-2}L^2L^{-3}} = \frac{L}{L^{-1}}$
Reduction with the variable: c^2	$\frac{(F)}{(\rho)(U^2)(L^2)} = \frac{L}{L\ L\ L^{-1}} = non\ dimensional$
First π term result:	$\pi_1 = \frac{F}{\rho\ v^2\ l^2}$

Only using the independent variables of the physical dimensions to match and reduce the dynamic viscosity (μ) physical dimensions, the second term is found and shown in Table 6.

Table 6. Dimensional analysis second term found.

Reduction with the variable: ρ	$\frac{(\mu)}{(\rho)} = \frac{ML^{-1}T^{-2}}{ML^{-3}} = \frac{T^{-1}}{L^{-2}}$
Reduction with the variable: U	$\frac{(\mu)}{(\rho)(U)} = \frac{T^{-1}}{L^{-2}\ L\ T^{-1}} = \frac{1}{L^{-1}}$
Reduction with the variable: c	$\frac{(\mu)}{(\rho)(v)(l)} = \frac{1}{L^{-1}L} = non\ dimensionnel$
Second π term result:	$\frac{1}{\pi_2} = \frac{\mu}{\rho\ v\ l} \rightarrow \pi_2 = \frac{\rho\ v\ l}{\mu}$

The first term π_1 is associated with the force produced by the wing surface versus the dynamic characteristics of the fluid. This dimensional term is associated with the lift coefficient C_l.

The second term π_2 is the ratio between the fluid inertial forces and the viscous forces inside the fluid. This term is associated with the Reynolds number (Re), and it is essential in wind tunnel testing because it allows the comparison of the fluid flow conditions between the full-scaled wings and the scaled-down models. The Buckingham theorem allows the finding of the relationship between the two π terms, which are thus proportional between the coefficients of the forces of lift and drag and the Reynolds number. The relationship is shown in Equation (4), where ∅ is the angle of the leading edge and the trailing edge.

$$\frac{F}{\rho\ v^2\ l^2} = \varnothing\left(\frac{\rho\ v\ l}{\mu}\right) \tag{4}$$

5.5. Dynamic Similitude with the Reynolds Number

The flow conditions for a prototype wing ($wing_{prot}$) and the UAV S45 original wing ($wing_{ref}$) can be reproduced if all the relevant parameters have the same values. The Reynolds numbers of the prototype and the original wing have to be equal to reproduce the aerodynamics forces and pressure coefficients during wind tunnel testing.

$$wing_{prot}\left\{\frac{\rho\ v\ l}{\mu}\right\} = wing_{ref}\left\{\frac{\rho\ v\ l}{\mu}\right\} \tag{5}$$

The $wing_{ref}$ has a chord length of 0.52 m and a cruising speed of 25.72 m/s.

The $wing_{prot}$ built in-house has a chord length of 0.445 m, which is smaller than $wing_{ref}$ due to the test section size and the maximum size of a model for wind tunnel tests, to reduce the "blockage effect", as described by Mehta et al. [22].

Solving the dynamic similitude Equation (5) gives a flow velocity for the wind tunnel tests of 30.10 m/s, as shown in Equations (6) and (7).

$$v_{prototype} \times 0.445\ m = 25.72\frac{m}{s} \times 0.52\ m \tag{6}$$

$$v_{prototype} = 30.10\frac{m}{s} \tag{7}$$

For the CFD simulations, the flow speed will be set precisely at 30.10 m/s. The wind tunnel test flow speed will be set at 30.1 m/s. The flow speed was measured with a pressure sensor connected to a Pitot tube with a sensor accuracy of ±0.05 m/s.

6. Adaptive Wing CFD Model

In this section, a simulation model must be designed and meshed for CFD calculations. The first step consists of the design of the geometry of the adaptive wing prototype in Figure 20 and that of the wind tunnel, as shown in Figure 3 in CATIA V5. The second consists of the geometries meshing using structured and unstructured mesh sizes on the model's surface, and the last step is the use of CFD solver to find the lift and drag forces [34]. A robust mesh model of the adaptive wing prototype was designed using an ANSYS ICEM mesh generator. The mesh volume of these two objects consists of a finite number of polygons composed of triangle and quad elements. Quad polygons have a better topology (how the polygons are connected to the flow around them) and a better resolution of the flow boundary conditions.

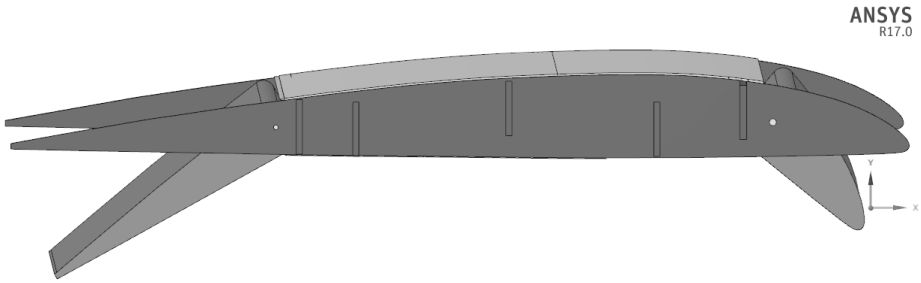

Figure 20. CFD model of the adaptive wing prototype.

For a wind tunnel CFD model, there are five boundary conditions that must be specified during the mesh design, and as well as in the CFD Solver: (i) the "inlet boundary condition", which is the surface where the flow is initiated, mainly when the flow speed in one of the axes (x, y, z) is specified; (ii) the "outlet boundary condition", which is the region where the flow attains a fully developed state and where no change in velocity or direction occurs far from the model disturbances; (iii) the "wall boundary condition", which defines the appropriate flow condition near the walls (inside the wind tunnel test chamber and at the surface of the model); (iv) the "Constant pressure boundary conditions", which are used when the inlet pressure is known and when the outlet pressure can be determined; in an open circuit wind tunnel, the outlet pressure is the atmospheric pressure; and (v) the "symmetric boundary condition", which is calculated when the same physical conditions exist on two sides of a model.

The designed CADs (step files) of the adaptive wing prototype and of the wind tunnel were imported to the ANSYS ICEM meshing software. The meshing process includes the (i) design of an initial mesh, followed by an evaluation of its quality and the boundary conditions specifications; (ii) the improvement and repairing of the mesh holes, discontinuities, and space between its cells; (iii) the generation of the volume mesh using triangle and quad elements and the refining of the mesh density close to its boundary layer; and (iv) the exportation of the final mesh to the CFD solver.

A mesh with an optimum grid resolution had to be refined along the model's surface. The fluid at the wing model surface, named "Inner_fluid", and the flow inside the wind tunnel have to be simulated together. The generated grids have coarse regions, and it was achieved using the octree method with "Tetra Cell". It was re-meshed using the Delaunay refinement mesh technique. The octree method allows the design of regular internal mesh geometry and does not require an initial mesh to be implemented. The Delaunay technique allows for a smoother mesh and a better accuracy in representing complex shapes.

A "grid sensitivity" study was conducted to determine the mesh density required to produce final results of acceptable fidelity. Grids of varying resolution were tested using the flight test number 22 (leading edge at -5° and trailing edge at -10°), the angle of attack of 3°, and the Reynolds number of 5.89×10^5, corresponding to a flow velocity of U = 30.10 m/s. The wall parameter $y^+ < 1$ was maintained regardless of the tested grid [35]. The variations of C_l, C_d and C_l/C_d are shown in Table 7. It can be observed that the results change significantly for the first three grid resolutions (Grid 1, 2, and 3); after the fourth and fifth grid resolutions (Grid 4 and 5), the mesh density does not significantly affect the results of the aerodynamics coefficients.

Table 7. Grid sensitivity results.

Grid Density	Quantity of Cells	C_l	C_d	C_l/C_d
1	900,542	0.02489	0.00920	2.70
2	1,325,584	0.02435	0.008665	2.81
3	1,854,000	0.02313	0.007896	2.92
4	2,258,477	0.022869	0.007584	3.02
5	3,524,648	0.022855	0.007545	3.03

There is a 1% error between the grid 4 and 5 results and a mesh size reduction of 1.266 million cells for grid 4, compared to the grid 5 density. Based on the Table 7 results, the grid 4 density will be used for all the adaptive wing simulations.

Figure 21 shows only the mesh volumes of the adaptive wing model. The main motivation for determining these grid sensitivity results is to reduce the computational time while obtaining accurate results.

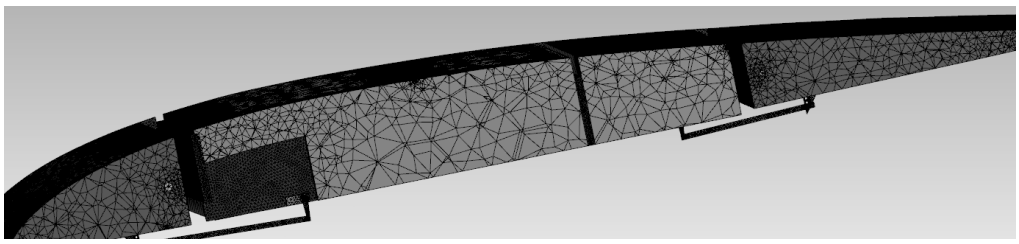

Figure 21. Mesh of the adaptive wing model.

The boundary conditions are required in CFD simulations to solve the differential equations for the fluid volume. An inlet surface allows the air mass to flow into the domain of the test velocity of 30.10 m/s, while a pressure outlet surface allows the air mass to flow out of this domain. Slip walls were imposed on the sides of the far field to improve the solution convergence, and a no-slip wall was enforced at the surface of the wing model to obtain a fluid velocity at its surface equal to zero. The simulation implicit solver had a time step size of 0.001 s, which was considered necessary for numerical stability, for which 400 total time steps were conducted to a converged solution at the residual target of 1×10^{-5} for all the flow and turbulence variables.

The CFD Fluent software was used to solve the adaptive wing model mesh, as described previously. The data obtained experimentally were compared with the "steady state" analysis results (simulations), but the errors and uncertainties were beyond the 10% validation metric limit, which will be explained in detail in Section 8.

A rigid wind model, with no moving parts, in a laminar flow regime can be accurately predicted by the steady state Navier–Stokes equations by assuming, at simulation convergence, that the local speeds do not vary with time. In the case of an adaptable wing, the simulations have to be solved in a transient state analysis. A transient state allows for an accurate representation of flow behavior. The flow turbulence intensity was kept at 1% and therefore at the same turbulence levels as in the Price–Païdoussis wind tunnel tests.

Selecting an accurate turbulence model for an accurate representation of wall-bounded flow, mild to important flow separation and recirculation, and flow transition is a challenging aspect in CFD simulations. The presence of a wing prototype with actuated/controlled leading edge and trailing edge surfaces generates additional turbulence characteristics to the flow regime in the test section.

Four RANS models were tested with the CFD solver: Spalart–Allmaras (SA), K-epsilon (K-ε), K-Omega (K-ω), and the shear stress transport (SST). The Spalart–Allmaras model is a single-equation model involving wall-bounded flows and a low Reynolds number [36]. The SA model produced an absolute error of 20% compared to the experimental loads. The K-epsilon two-transport equation model solves for kinetic energy k and dissipation ε, where dissipation is the rate at which the velocity fluctuations dissipate [37]. It uses coefficients that are found empirically, and it was found that the K-epsilon model is accurate for unsteady flow regimes. The absolute errors with the experimental loads were within the 10% validation limit. The K-Omega is a two-variables model, used to obtain the kinetic energy k and frequency ω. This model allows for a more accurate near-wall treatment and demonstrates superior performance for wall-bounded and low Reynolds number flows and for predicting transition [38]. The absolute errors between the experimental and the simulated loads were within the 10% validation limits. The shear stress transport (SST) model is a variant of the standard K–Omega model; it combines the original Wilcox k-Omega model for use near walls and the standard K-epsilon on the regions far from the walls [39,40]. This model has been proven to offer high accuracy on the boundary layer regions, but it does not converge to a solution quickly. Therefore, the initial conditions of the simulation were solved with the K-Omega model to improve the conversion rate. The absolute errors between the experimental and the simulated loads were below the 5% validation limits. The adaptive wing model was simulated with the SST model.

7. Experimental Data and Model Validation

The CFD models do not always reproduce data accurately, and there are many sources of errors in the simulation results. Due to these errors, model verification and validation is a research requirement to obtain accurate simulations with quantified uncertainties [41,42]. The 2012 ASME committee provides a useful validation approach for cases when experimental data are available. Even though no specific metric is imposed, the guide recommends using a single metric to better quantify the difference between the simulation and the experimental data. The metric must measure the difference between the experimental outcomes and the simulation outcomes; it should be equal to zero if the outcomes are identical, and it should provide a coherent numerical value expressing the model's accuracy and adequacy. The area metric method proposed by Ferson et al. [43] allows the comparison of the simulation results with the experimental data.

Table 8 presents the S45 wing parameters and flow conditions allowing the calculation of the aerodynamics coefficients of the lift and drag and the lift-to-drag ratio. Consequently, it would be possible to compare the S45 performances with the wing prototype experimental data.

The 29 wind tunnel tests results (lift and drag forces) are presented in Table 9, and they show a very good agreement with the simulation values. The wind tunnel tests are sorted by the angular position of the adaptive leading edge. In total, 29 wind tunnel tests were performed, and the two forces of lift and drag were measured by the aerodynamic scale.

7.1. Residual Analysis of the Lift and Drag Forces

The observed and predicted lift and drag quantities were very close, as shown in the residual errors in Table 10. As mentioned in the ASME validation guidelines, a simulated CFD model should be able to predict up to 85% of the experimental output, with less than 5% error [44]. This means that for this project with 29 simulation and wind tunnel tests (Table 9), the validation guidelines require ($29 \times 85\% = 24.6$) that at least 24 simulations results have 5% or less difference (error) with the experimental data.

Table 8. Aerodynamic parameters of the S45 reference wing.

Flow Conditions	
Velocity Flow (m/s)	30.1
Density air (kg/m^3)	1.225
Temperature (°C)	22
Wing structure	
Wingspan (m)	0.495
Wing chord (m)	0.455
Wing surface (m^2)	0.2252
Experimental data	
Lift force (N) =	1.942
Drag force (N) =	0.644
C_l =	0.022869
C_d =	0.007584
$\frac{L}{D}$ =	3.02

Table 9. Experimental and simulated data of the adaptive wing prototype.

Test	**Adaptive Wing Surfaces**		**Experimental**		**Simulation**	
	Leading Edge (Degrees)	**Trailing Edge (Degrees)**	**Wind Tunnel**		**CFD Model**	
			L_{exp} (N)	**D_{exp} (N)**	**L_{sim} (N)**	**D_{sim} (N)**
1	0	0	1.942	−0.644	1.5885	−0.6457
2	−5	0	1.839	−0.67	1.4504	−0.6637
3	−10	0	1.676	−0.736	1.3584	−0.6817
4	−15	0	1.484	−0.84	1.2723	−0.8780
5	−20	0	1.359	−0.865	1.1917	−0.8960
6	5	0	2.011	−0.618	1.7083	−0.5690
7	10	0	2.197	−0.678	1.8239	−0.5510
8	15	0	2.254	−0.713	1.9474	−0.7460
9	20	0	2.26	−0.729	2.0792	−0.7750
10	0	−5	2.293	−0.701	2.0833	−0.4341
11	0	−10	2.769	−0.759	2.5740	−0.5186
12	0	−15	3.506	−0.908	3.0948	−0.6004
13	0	−20	4.199	−1.046	3.6680	−0.6780
14	0	−25	4.784	−1.135	4.3163	−0.7687
15	0	−30	5.502	−1.295	5.0620	−0.8469
16	0	5	2.029	−0.604	0.9018	−0.2779
17	0	10	1.142	−0.549	0.3660	−0.1897
18	0	15	0.216	−0.45	−0.2298	−0.1040
19	0	20	−0.532	−0.404	−0.9080	−0.0286
20	0	25	−1.222	−0.296	−1.6913	0.0501
21	0	30	−1.811	−0.243	−2.6020	0.1420
22	−5	−10	1.43	−0.988	2.0148	−0.6457
23	−10	−15	2.971	−1.165	3.1309	−0.4750
24	−15	−20	4.182	−1.306	4.2898	−0.9360
25	−20	−30	4.987	−1.131	5.2796	−0.9540
26	5	10	2.441	−0.734	2.5712	−0.5455
27	10	15	1.051	−0.486	1.1005	−0.6457
28	15	20	−0.201	−0.468	−0.2096	−0.6637
29	20	30	−0.724	−0.349	−0.7706	−0.6817

Table 10. Residual values of the experimental and simulated lift and drag forces.

Test	Residual Lift (N)	Residual Drag (N)
1	0.35	0.00
2	0.39	−0.01
3	0.32	−0.05
4	0.21	0.04
5	0.17	0.03
6	0.30	−0.05
7	0.37	−0.13
8	0.31	0.03
9	0.18	0.05
10	0.21	−0.27
11	0.20	−0.24
12	0.41	−0.31
13	0.53	−0.37
14	0.47	−0.37
15	0.44	−0.45
16	1.13	−0.33
17	0.78	−0.36
18	0.45	−0.35
19	0.38	−0.38
20	0.47	−0.35
21	0.79	−0.39
22	−0.58	−0.34
23	−0.16	−0.69
24	−0.11	−0.37
25	−0.29	−0.18
26	−0.13	−0.19
27	−0.05	0.16
28	0.01	0.20
29	0.05	0.33

The residuals of the lift and drag forces are defined as the differences between the observed values during the wind tunnel tests and the estimated values by the CFD simulation. Mathematically, the residual r of a specific value is the difference between the observed response value y and the predicted response value $\hat{y}$. The residuals should be scattered randomly and centered on zero throughout the range of the fitted values. The non-random pattern in the residuals indicates a calibration error or a bias during the experimental tests or an inadequate model. The Fluent simulation accurately captures the interaction of the adaptive wing model with the fluid, as shown in the values of the residuals in Table 10.

The residuals for the lift and drag forces appear to be random and distributed above and below the 0 error values, respectively. The differences between the experimental and the predicted values are independent and normally distributed, following a normal law with a mean value equal to zero and a very low variance. The residual values were calculated from the values shown in Table 10. The sum of the residuals shows that they are symmetric around the "zero" value.

7.2. Validation Method Durbin–Watson Test and Adjusted R^2

Figure 22 shows a quartile graph in which the drag residuals follow a line (at 45 degrees), indicating that its "different" values are distributed according to a normal law. The Durbin–Watson test predicts whether there is correlation in the order of appearance of the residuals for the drag force; given that the probability is 0.016% and less than 0.05%, there is evidence of correlation at a confidence level of 95%. We can reject the H_0 hypothesis (H_0 = there is no correlation between the residual drag values). The data show in Figure 23 show that the residuals for the lift force follow a normal distribution, and the histogram graph indicates a leftward bias.

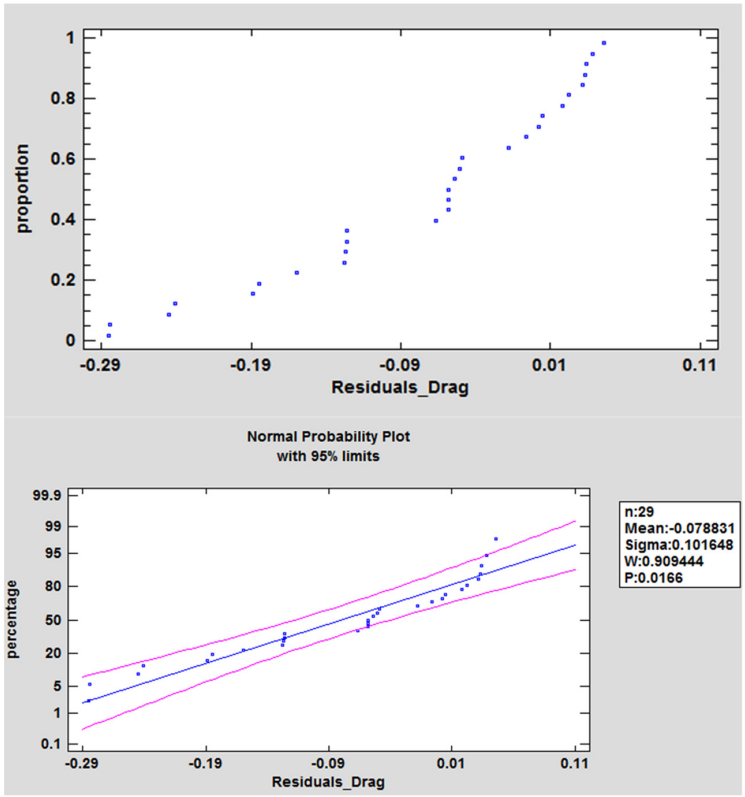

Figure 22. Analysis of the drag forces' residual values between the wind tunnel and model data.

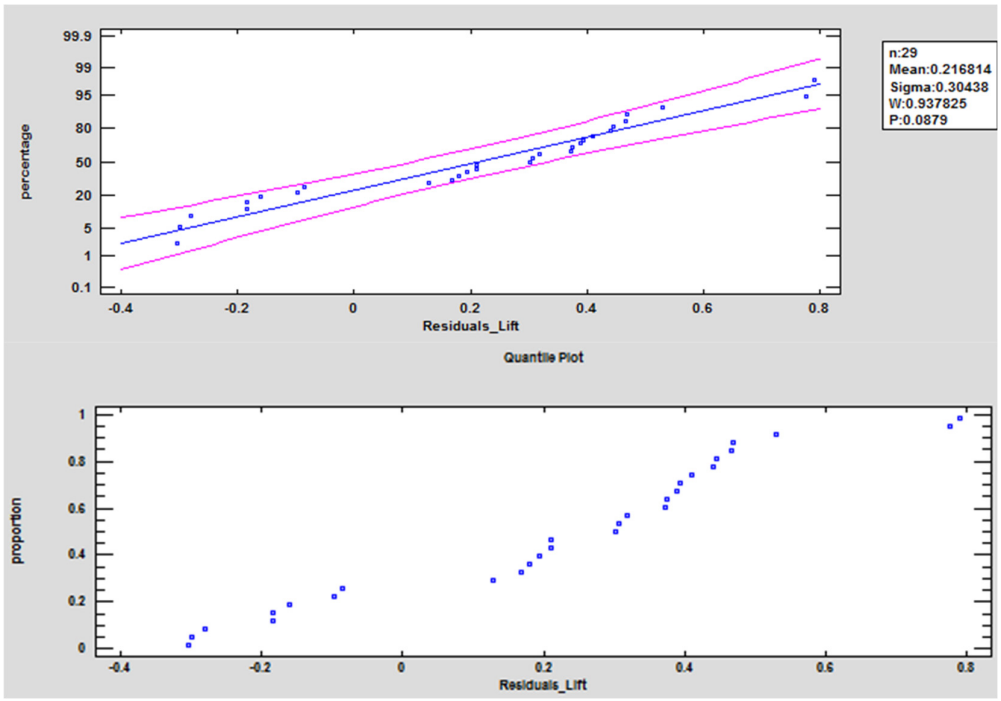

Figure 23. Analysis of the lift forces' residual values between the wind tunnel and model data.

Linear regression analysis with adjusted R^2 is a statistical process that focuses on the relationships between sets of variables; in this case, the regression analysis allows for an estimation of the difference between the model's predicted values and the experimental values. The predicted and observed data are numerically sorted from small to large; the model data are placed on the x-axis and the observed data on the y-axis [45,46]. A line with

a 45° slope is added to the plot where the dispersed data are shown. This line represents the ideal outcome where all the predicted values are 100% identical to the observed values. The magnitude of the correlation between the response and the predicted values can be quantified by calculating the adjusted R^2 (R-squared) of the model. This value denotes the proportion of the variance in the experimental data, which is predicted by the model data. An adjusted R^2 of 1 indicates that the model predicts all the experimental data perfectly, but in the real world, the models are never perfect, and the adjusted R^2 values may take any value from 0 to less than 1.

This method shows in Figure 24 that the model predicted the lift and drag forces values within the 95% bounds for the linear regression method. The adjusted R^2 values are 0.9986 for the lift and 0.9945 for the drag forces, thus indicating that the predictions of the variance for the lift force are 99.86% and 99.45% for the drag force, as accounted for by the model predictions and as seen in Figures 22 and 23, respectively.

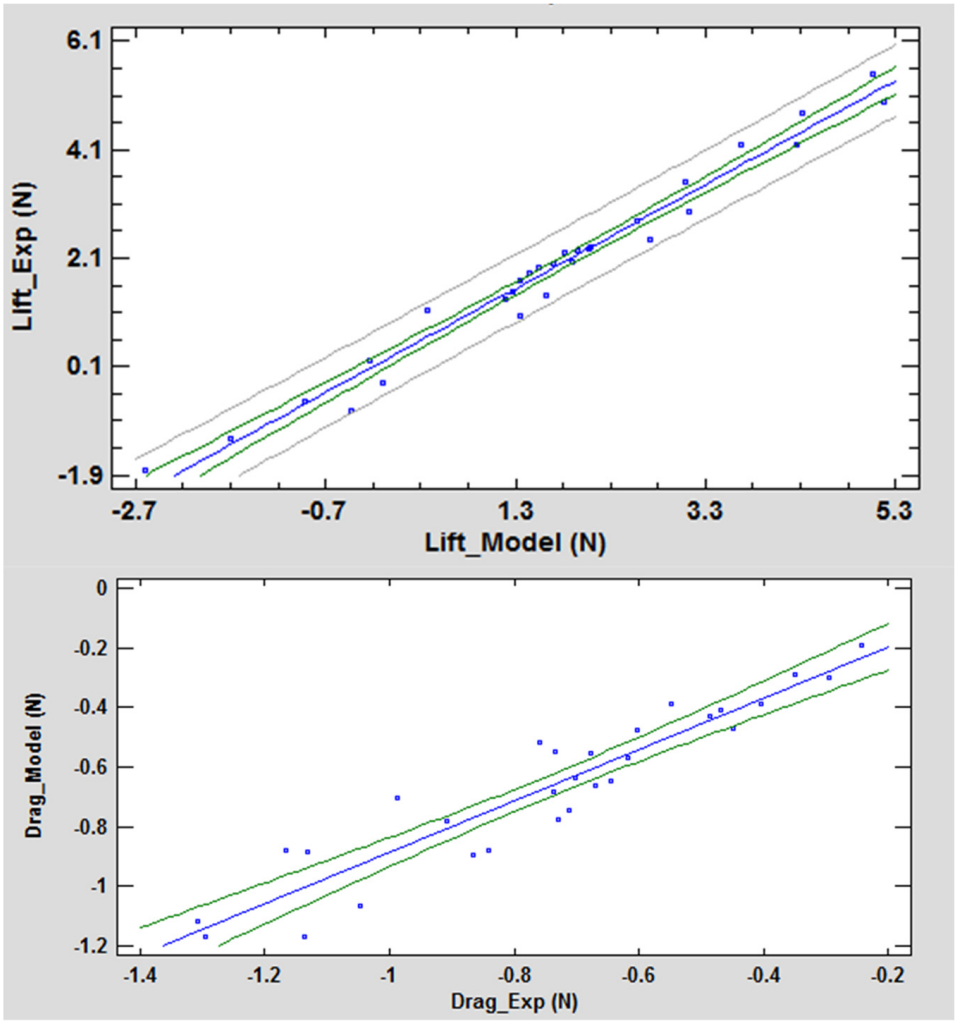

Figure 24. Analysis of the lift and drag data with the adjusted R^2 validation method.

To validate a statistical hypothesis on a group of data, if we set H_0 as the observed values and the simulated values from the same population, it is possible to assess at a confidence level of 95% whether this hypothesis is rejected or accepted. The weakness of this type of validation is that it is qualitative and not quantitative. This type of validation is mostly used to reject a model rather than to validate it at a high level of confidence [47].

The adjusted R^2 for the drag forces are strong and indicate that 87.24% of the experimental data can be explained by the model. The Durbin–Watson test makes it possible to check the correlation between the observed drag values and the simulated drag values. In this case, the test has a *p*-value much lower than its 0.05% threshold, which indicates a strong correlation. This hypothesis test does not reject H_0; so, the model is adequate for estimating drag forces. The adjusted R^2 for the lift forces indicates that the model represents 97.27% of the observed data. For the lift forces, the hypothesis test shows that there is a strong correlation between both results values, while the hypothesis H_0 cannot be rejected with a confidence level of 95%.

The validation tests were conclusive, thus indicating that the CFD model can simulate lift and drag forces at a 95% confidence level. The drag force residuals appear to have an autocorrelation, possibly due to the non-linearity of the range of observed values. These experimental values have an uncertainty of $\pm$0.04N, estimated at a confidence level of 95%.

The simulation model of the adaptive wing prototype was validated by the Durbin–Watson and adjusted R^2 tests, and it can be used to obtain accurate aerodynamics lift and drag forces.

7.3. Validation Method of the Area Metric for the Drag and Lift Forces

The area metric is the method recommended by ASME in their validation guidelines as being well-suited for the experimental research [48,49]. This method does conclude that a model is accepted or rejected, and it also allows the model validation to be quantified. The area metric method uses the cumulative probability of the observed data and the simulated values and calculates the integral (using the trapezium method) obtained for the surface of the observed values and the simulated values. The difference in the surfaces (between the curves) gives the value of the quantified metric in the same units as the analyzed data.

Comparing the curves obtained from the physical experiments with those given by the mathematical models is an important technique used by researchers to determine whether a model adequately represents the physical phenomena. This method allows the validation of a simulation model when only a limited number of experimental values can be measured, which is an advantage over the other validation methods.

Due to its quantitative measure of the discrepancy between all the data available (predicted data and observed data), the area metric offers an important advantage compared to classical validation methods; it is considered objective and robust [49] in producing a graphical representation of the discrepancy in the same physical units as the experimental data, and this makes it possible to evaluate the differences across the full range of prediction results while considering simulation uncertainties.

The area metric is calculated with the cumulative distribution function (CDF) of the experimental data and that of the model data. Both CDFs are step functions. Figures 25 and 26 illustrate the mismatch between the prediction distribution (shown in the "red" line) and the experimental data (shown in the "blue" line), with the area metric shown as the grey shaded area. This metric response has a value of 0.056N for the drag force. With the area metric, it is possible to check the adequacy of the model locally (on a specific point of the experimental test) or globally, by evaluating the difference value of 1.44N, for the lift forces.

The model validation process was conducted using three methods recommended by the ASME. The residuals, the adjusted R^2, and the area metric validation methods agree that the CFD model accurately estimates the lift and drag forces of the adaptive leading edge wing prototype. The model gave a 98% prediction rate, which is above the prediction rate of 85% recommended by ASME.

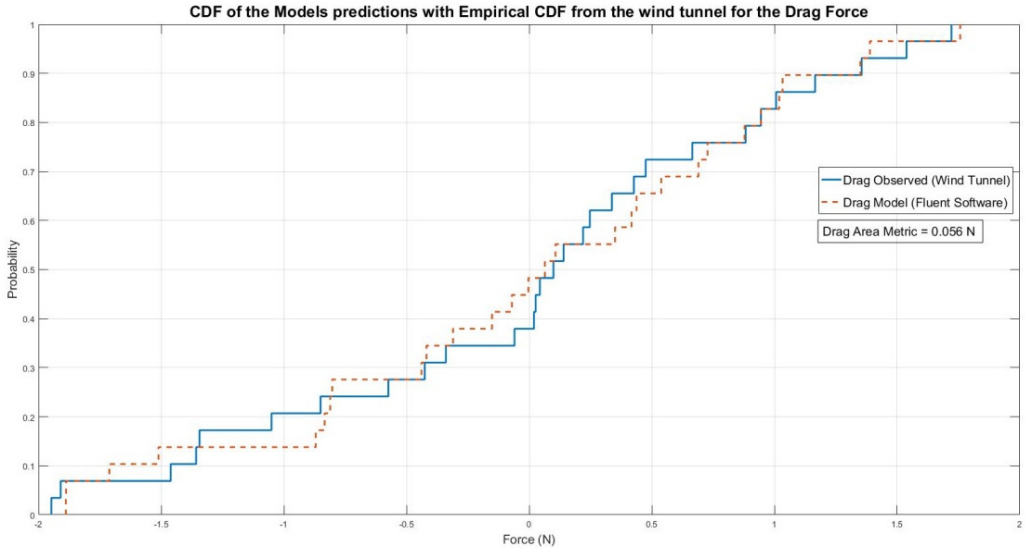

Figure 25. Area metric results for drag forces.

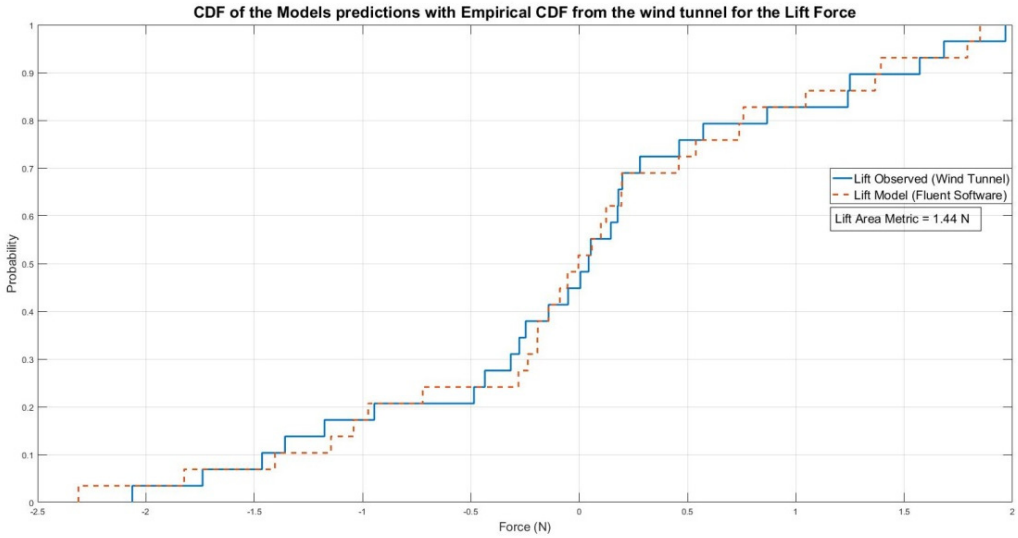

Figure 26. Area metric results for lift forces.

8. Conclusions

The study of the current "state of the art" of adaptive wings systems capable of improving the overall performance at subsonic speeds of UAVs was investigated as part of the literature review of this paper. It is thought by the authors that the present validation methodology on adaptive UAV wings will further improve the knowledge in this field. In this paper, a new validation methodology was developed to improve UAV aerodynamic performance during the cruise flight, by means of the model design, fabrication, simulation, and model validation of an adaptive wing prototype for the UAV S45. An adaptive wing was designed and validated using the proposed multidisciplinary methodology to find its optimized wing shapes that are able to improve the lift and drag performance during cruising phase. The main objective of this article was to develop a validation framework for an adaptive wing.

Aircraft design disciplines, airfoil shape optimization, computational simulations, and wind tunnel tests were integrated into this framework. The CFD models allowed us to obtain the aerodynamic performances of the wing equipped with an adaptive leading edge and trailing edge.

The verification and validation of the CFD model with an accurate mesh grid and the area metric method were successfully performed. The simulation results obtained, with

the specific flow conditions defined in the wind tunnel tests, accurately agree with the experimental studies.

The authors have used the term "New knowledge" in the abstract as we believe that the MDO methodology and the CFD model validation presented in this study both correspond to "a novel research outcome" on improving the performance of adaptive wings.

The results of the adaptive wing system can be seen in Figure 27, where the lift-to-drag ratios can increase compared to the S45 original wing shape value of $L/D = 3$. The wind tunnel results show the efficiency of the adaptive wing prototype in producing less drag and more lift, resulting in higher L/D values, depending on the configuration of the actuators. This prototype wing can produce an important lift-to-drag ratio without extra fuel consumption from the UAV's engine. The $L/D = 7.5$ for test #21 is at the maximum displacement of the actuators but within the safety structural parameters of the prototype.

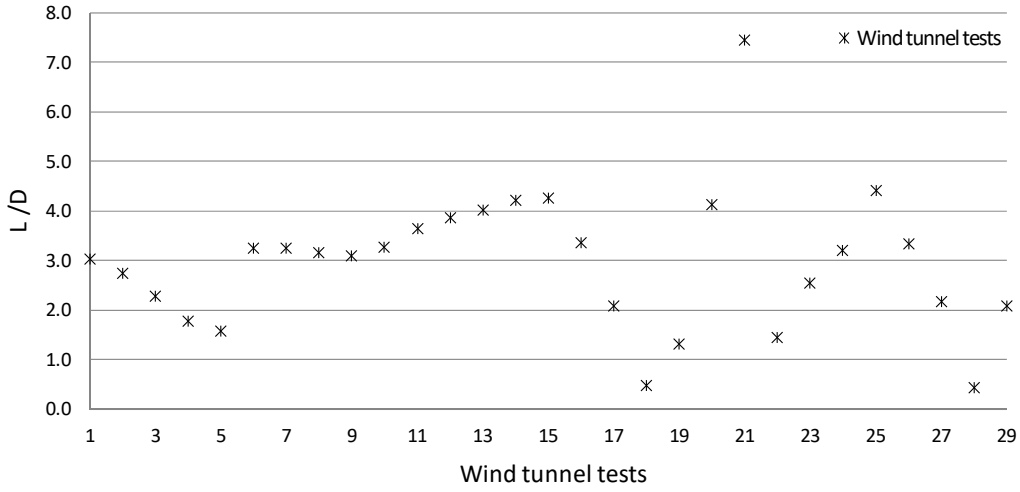

Figure 27. Lift-to-drag wind tunnel results of the adaptive wing prototype at cruising speed of 30.1 m/s.

The low drag production and high lift-to-drag ratio (efficiency factor) of the adaptive wing will translate into a reduction in fuel consumption and an increase in the S45 effective range. Adaptive wing systems for UAVs are a promising technology and have become a major solution for multipurpose flight operations because they allow the aerodynamic potential of UAVs to be optimized by adapting the wing to several flight conditions, and they also result in climate improvement by fuel consumption minimization.

Author Contributions: M.F.S.: investigation, experimental tests, analysis, writing—original draft; R.M.B.: supervision, review and editing; G.G.: review. All authors have read and agreed to the published version of the manuscript.

Funding: Canada Research Chairs NSERC Program; 231679.

Acknowledgments: The authors would like to express their thanks to Michael Païdoussis and Stuart Price for the donation of the Price–Païdoussis Open Return Subsonic Wind Tunnel at the LARCASE research laboratory at École de technologie supérieure. The authors gratefully acknowledge the financial support by the Natural Sciences and Engineering Research Council of Canada (NSERC).

Conflicts of Interest: The authors declare no conflict of interest. The authors declare that they have no known competing financial interest or personal relationships that could have appeared to influence the work reported in this paper.

References

1. Ameduri, S.; Concilio, A. Morphing wings review: Aims, challenges, and current open issues of a technology. *Proc. Inst. Mech. Eng. Part C J. Mech. Eng. Sci.* **2020**, 0954406220944423. [CrossRef]
2. Giuliani, M.; Dimino, I.; Ameduri, S.; Pecora, R.; Concilio, A. Status and Perspectives of Commercial Aircraft Morphing. *Biomimetics* **2022**, *7*, 11. [CrossRef] [PubMed]

3. Pecora, R. Morphing wing flaps for large civil aircraft: Evolution of a smart technology across the Clean Sky program. *Chin. J. Aeronaut.* **2021**, *34*, 13–28. [CrossRef]
4. Dimino, I.; Lecce, L.; Pecora, R. *Morphing Wing Technologies: Large Commercial Aircraft and Civil Helicopters*; Butterworth-Heinemann: Oxford, UK, 2017.
5. Suzuki, S.; Yonezawa, S. Simultaneous structure/control design optimization of a wing structure with a gust load alleviation system. *J. Aircr.* **1993**, *30*, 268–274. [CrossRef]
6. Haghighat, S.; Martins, J.R.; Liu, H.H. Aeroservoelastic design optimization of a flexible wing. *J. Aircr.* **2012**, *49*, 432–443. [CrossRef]
7. Arena, M.; Concilio, A.; Pecora, R. Aero-servo-elastic design of a morphing wing trailing edge system for enhanced cruise performance. *Aerosp. Sci. J.* **2019**, *86*, 215–235. [CrossRef]
8. Gundlach, J. *Designing Unmanned Aircraft Systems: A Comprehensive Approach*; American Institute of Aeronautics and Astronautics, Inc.: Reston, VA, USA, 2012.
9. Sadraey, M.H. *Aircraft Design: A Systems Engineering Approach*; John Wiley & Sons: Hoboken, NJ, USA, 2012.
10. Lee, H.; Sengupta, B.; Araghizadeh, M.S. Review of vortex methods for rotor aerodynamics and wake dynamics. *Adv. Aerodyn.* **2022**, *4*, 20. [CrossRef]
11. Valasek, J. (Ed.) *Morphing Aerospace Vehicles and Structures*; John Wiley & Sons: Hoboken, NJ, USA, 2012.
12. Liebeck, R.H. Design of the blended wing body subsonic transport. *J. Aircr.* **2004**, *41*, 10–25. [CrossRef]
13. Monner, H.P.; Breitbach, E.; Bein, T.; Hanselka, H. Design aspects of the adaptive wing—The elastic trailing edge and the local spoiler bump. *Aeronaut. J.* **2000**, *104*, 89–95. [CrossRef]
14. Sofla, A.Y.; Meguid, S.A.; Tan, K.T.; Yeo, W.K. Shape morphing of aircraft wing: Status and challenges. *Mater. Des.* **2010**, *31*, 1284–1292. [CrossRef]
15. Popov, A.V.; Botez, R.M.; Labib, M. Transition point detection from the surface pressure distribution for controller design. *J. Aircr.* **2008**, *45*, 23–28. [CrossRef]
16. Grigorie, L.T.; Botez, R.M.; Popov, A.-V. How the Airfoil Shape of a Morphing Wing is Actuated and Controlled in a Smart Way. *J. Aerosp. Eng.* **2015**, *28*, 04014043. [CrossRef]
17. Grigorie, L.T.; Botez, R.M. Control strategies for an experimental morphing wing model. In Proceedings of the AIAA Atmospheric Flight Mechanics Conference, National Harbor, MD, USA, 13–17 January 2014; p. 2187.
18. Botez, R.M.; Grigorie, T.L.; Khan, S.; Mamou, M.; Mebarki, Y. A smart controlled morphing wing experimental model with the structure based on a full-scaled portion of a real wing. In Proceedings of the AIAA Scitech 2021 Forum, online, 11–22 January 2021; p. 1836.
19. Sugar Gabor, O.; Koreanschi, A.; Botez, R.M.; Mamou, M.; Mébarki, Y. Numerical Simulation and Wind Tunnel Tests Investigation and Validation of a Morphing Wing-Tip Demonstrator Aerodynamic Performance. *Aerosp. Sci. Technol.* **2016**, *53*, 136–153. [CrossRef]
20. Tchatchueng Kammegne, M.J.; Grigorie, L.T.; Botez, R.M.; Koreanschi, A. Design and Wind Tunnel Experimental Validation of a Controlled New Rotary Actuation System for a Morphing Wing Application. *Proc. Inst. Mech. Eng. Part G J. Aerosp.* **2016**, *230*, 132–145. [CrossRef]
21. Salinas, M.F.; Botez, R.M.; Gauthier, G. New numerical and measurements flow analyses near radars. *Appl. Mech.* **2021**, *2*, 303–330. [CrossRef]
22. Mehta, R.D.; Bradshaw, P. Design rules for small low speed wind tunnels. *Aeronaut. J.* **1979**, *73*, 443–449.
23. Katoch, S.; Chauhan, S.S.; Kumar, V. A review on genetic algorithm: Past, present, and future. *Multimed. Tools. Appl.* **2021**, *80*, 8091–8126. [CrossRef]
24. Koreanshi, A.; Sugar Gabor, O.; Acotto, J.; Brianchon, G.; Portier, G.; Botez, R.M.; Mamou, M.; Mebarki, Y. Optimization and design of a morphing wing tip aircraft demonstrator for drag reduction at low speed, part I-Aerodynamic optimizations using genetic, bee colony and gradient descent algorithms. *Chin. J. Aeronaut.* **2017**, *30*, 149–163. [CrossRef]
25. Roskam, J. *Airplane Design Part I: Preliminary Sizing of Airplanes, Design, Analysis and Research Corporation*; DARCorporation: Lawrence, KS, USA, 2005.
26. Raymer, D. *Aircraft Design: A Conceptual Approach*; AIAA: Washington, DC, USA, 2012.
27. Communier, D.; Salinas, M.F.; Carranza Moyao, O.; Botez, R.M. AeroStructural Modeling of a Wing using CATIA V5 and XFLR5 Software and Experimental Validation using the Price-Païdoussis Wind Tunnel. In Proceedings of the AIAA Atmospheric Flight Mechanics Conference, AIAA Aviation, Kissimmee, FL, USA, 5–9 January 2015; p. 2558.
28. Concilio, A.; Ciminello, M.; Galasso, B.; Pellone, L.; Mercurio, U.; Apuleo, G.; Cozzolino, A.; Kressel, I.; Shoham, S.; Bardenstein, D. De-Bonding Numerical Characterization and Detection in Aeronautic Multi-Element Spars. *Sensors* **2022**, *22*, 4152. [CrossRef]
29. Lo, S.H.; Lee, C.K. On using meshes of mixed element types in adaptive finite element analysis. *Finite Elem. Anal. Des.* **1992**, *11*, 307–336. [CrossRef]
30. Grisval, J.P.; Liauzun, C. Application of the finite element method to aeroelasticity. *Rev. Eur. Élém. Finis.* **1999**, *8*, 553–579. [CrossRef]
31. Bendler, J.T. *Handbook Of Polycarbonate Science and Technology*, 1st ed.; CRC Press: New York, NY, USA, 1999; p. 374.
32. Mendez, P.; Ordonez, F. Scaling Laws from Statistical Data and Dimensional Analysis. *J. Appl. Mech.* **2005**, *72*, 648–657. [CrossRef]

33. Cheng, Y.T.; Cheng, C.M. Scaling, dimensional analysis, and indentation measurements. *Mater. Sci. Eng. R Rep.* **2004**, *44*, 91–149. [CrossRef]
34. Liauzun, C. Aeroelastic Response to Gust Using CFD Techniques. In Proceedings of the 3rd Joint US-European Fluids Engineering Summer Meeting Collocated with 8th International Conference on Nanochannels, Microchannels, and Minichannels, Montreal, QC, Canada, 1–5 August 2010; ASME: New York, NY, USA, 2010; pp. 269–276.
35. Katz, A.; Sankaran, V. Mesh quality effects on the accuracy of CFD solutions on unstructured meshes. *J. Comput. Phys.* **2011**, *230*, 7670–7686. [CrossRef]
36. Spalart, P. Strategies for turbulence modelling and simulations. *Int. J. Heat Fluid Flow* **2000**, *21*, 252–263. [CrossRef]
37. Durbin, P.A. Separated Flow Computations with the k-e-v2 Model. *AIAA J.* **1995**, *33*, 659–664. [CrossRef]
38. Launder, B. Turbulence modelling for C.F.D. By DC Wilcox. *J. Fluid Mech.* **1995**, *289*, 406–407. [CrossRef]
39. Menter, F. Review of the shear-stress transport turbulence model experience from an industrial perspective. *Int. J. Comut. Fluid Dyn.* **2009**, *23*, 305–316. [CrossRef]
40. Jameson, A.; Martinelli, L.; Pierce, N.A. Optimum aerodynamic design using the Navier–Stokes equations. *Theor. Comput. Fluid Dyn.* **1998**, *10*, 213–237. [CrossRef]
41. Oberkampf, W.L.; Trucano, T.G. Verification and validation in computational fluid dynamics. *Prog. Aerosp. Sci.* **2002**, *38*, 209–272. [CrossRef]
42. Huvelin, F.; Dequand, S.; Lepage, A.; Liauzun, C. On the validation and use of high-fidelity numerical simulations for gust response analysis. *AerospaceLab J.* **2018**, *14*, 1–16.
43. Ferson, S.; Oberkampf, W.L.; Ginzburg, L. Model validation and predictive capability for the thermal challenge problem. *Comput. Methods Appl. Mech. Eng.* **2008**, *197*, 2408–2430. [CrossRef]
44. Holger, D.; Munk, A. Validation of Linear Regression Models. *Ann. Stat.* **1998**, *26*, 778–800.
45. Rawlings, J.; Pantual, S.; Dickey, D. *Applied Regression Analysis: A Research Tool*, 2nd ed.; Springer Texts in Statistics; Springer: New York, NY, USA, 1998.
46. Devore, J. *Probability and Statistics for Engineering and the Physical Sciences*; Brooks/Cole Publ.: Salt Lake City, UT, USA, 1982.
47. Liu, Y.; Chen, W.; Arendt, P.; Huang, H.Z. Toward a better understanding of model validation metrics. *J. Mech. Des.* **2011**, *133*, 071005. [CrossRef]
48. Chatenet, Q.; Tahan, A.; Gagnon, M.; Chamberland-Lauzon, J. Numerical model validation using experimental data: Application of the area metric on a Francis runner. *IOP Conf. Ser. Earth Environ. Sci.* **2016**, *49*, 062015. [CrossRef]
49. Wang, N.; Yao, W.; Zhao, Y.; Chen, X.; Zhang, X.; Li, L. A new interval area metric for model validation with limited experimental data. *J. Mech. Des.* **2018**, *140*, 061403. [CrossRef]